Towards current-induced magnetization switching with a 100% spin-polarized current

THESIS

submitted in partial fulfillment of the
requirements for the degree of

MASTER OF SCIENCE
in
PHYSICS

Author :	Louis Maduro
Student ID :	s0964034
Supervisor :	Drs. Kaveh Lahabi
	Prof. Dr. Jan Aarts
2^{nd} corrector :	Dr. M.P Allan

Leiden, The Netherlands, June 8, 2016

Towards current-induced magnetization switching with a 100% spin-polarized current

Louis Maduro

Huygens-Kamerlingh Onnes Laboratory, Leiden University
P.O. Box 9500, 2300 RA Leiden, The Netherlands

June 8, 2016

Abstract

The magnetic state of a ferromagnet can be manipulated using a spin-current. This thesis is an attempt to switch the magnetization of a nanomagnet using a 100% spin-polarized current provided by the half-metallic CrO_2. We aim to realise this in nanopillars consisting of CrO_2 and a free magnetic layer. The main focus is on the fabrication challenges and finding the optimal device configuration. Micromagnetic simulations on CrO_2, Co, and Ni systems were used to investigate this.

Chapter 1

Introduction

The phenomena of magnetism has been known to man since ancient times. Over the centuries our understanding of magnetism has evolved from metaphysics to its recent quantum mechanical description[1] [2]. It is not quite clear who discovered magnetism, or created the first piece of magnetic technology. There is however no doubt about the increasingly vital role magnetics takes in today's fast growing technologies. [3]. In conventional electronics the spin degree of freedom is generally ignored and the charge degree of freedom is used to conduct logic operations. *Spintronics* is a rapidly emerging field of electronics and is perhaps one of the most prominent branches of magnetics. Its main focus is to utilise the spin degree of freedom to execute logic operations in a similar manner as conventional electronics. The realization of spintronic devices became possible with the discovery of giant magnetoresistance (GMR). Giant magnetoresistance can be observed by passing a current through two ferromagnets, which are separated by a non-magnetic metallic spacer. The resistance depends on the relative orientation of the magnetization between the two ferromagnets. It turns out that parallel alignment of the magnetization of the two ferromagnets leads to a minimum in the resistance of the device, while anti-parallel alignment results in a maximum in the resistance. This huge increase in resistance, typically in the 10% range[4], is named the Giant Magnetoresistance effect[5]. If the relative orientation of the magnetization of the two layers is in between parallel and anti-parallel alignment, then the measured resistance is also between the mnimum and maximum resistance, respectively. Hard disk drive (HDD) heads is one application of the GMR effect. The detection of an electrical current is pos-

sible with the help of magnetic field sensors. Magnetic field sensors are a series of GMR based magnetic sensors and switches which can be used as biosensors for measuring blood flow[3]. Magnetic tunnel junctions (MTJ) can also be used to improve HDD read heads. Typically, a non-magnetic metal layer is placed between the two magnetic layers in GMR devices. In MTJ the non-magnetic metal layer is replaced with an insulating tunnel barrier[6]. Spins from one magnetic layer have a higher probabillity of tunneling through to the other magnetic layer if the magnetizations are parallel as compared to other relative orientations of the magnetizations of the two magnetic layers.

A spin current (which can be either a spin-polarized current, or carry no charge at all) carries angular momentum, which can be used to manipulate the magnetization of a mesoscopic magnet, which is known as spin-transfer torque. This provides a unique opportunity for developing magnetic memory elements that can be efficiently controlled solely by a current. Spintronics can be combined with existing electronic technologies along with photonic technologies, effectively unifying three important fields in information technology. Transfer of data is possible by connecting the electron spin to the photon chirality (helicity), while an assembly of spins can be used for data storage[3]. Another promising application is the creation of spin-torque nano-oscillators. Precession of the magnetization of the free layer is possible if a large enough spin-polarized current is sent through the free layer. The precession of the magnetization of the free layer thus leads to resistance oscillations, due to the magnetoresistance[4][3][7]. The d.c. current thus induces a.c. voltage oscillations[8] [9]. The nano-oscillators can be used in signal-processing, as they are highly tunable, agile, and highly integrable. Large bandwidths of frequency modulation is also possible. Other applications of spin-polarized currents include the fabrication of spin valves[3] or studies of domain wall motion[10] [11], which can result in the fabrication of racetrack memory devices.

In current-induced-magnetization-switching (CIMS) devices, the magnetization of a ferromagnet is manipulated by a spin-polarized current. The spin-polarized current exerts a torque on the ferromagnet and if the current is sufficiently large it can cause a permanent change in the orientation of the magnetization of the ferromagnet. It is thus important to know at what value of the current the magnetization is switched, the critical current density J_C. The critical current density for a monodomain magnetic

body is given by [12],

$$J_C = \frac{\alpha}{\eta}\left(\frac{2e}{\hbar}\right)(l_m H_k M_s)\left(1 + \frac{2\pi M_s}{H_k} + \frac{H}{H_k}\right) \tag{1.1}$$

where l_M is the thickness of the switching layer, H is the applied field strength, M_s is the saturation magnetization, H_k is the uniaxial anisotropy field, and η is the spin-polarization. Although the theoretical framework for spin-transfer torque was developed by Slonczewski [13] and Berger [14] in 1996, there still remains crucial challenges in optimally utilizing this in functional devices. Typical values for the critical current density are in the range $\sim 10^7$ A/cm^2[7]. It is obvious from Eq. 1.1 that the critical current density can be lowered in several ways. Yagami *et al.* used a CoFeB layer as the free layer since it has a low saturation magnetization M_s[15]. They compared the critical current densities for Co-Fe_{25}/Cu/Co-Fe_{25} and another structure where the Co-Fe_{25} free layer was replaced with CoFeB. For the Co-Fe_{25} free layer structure the average critical current density was $\sim 4 \times 10^7$ A/cm^2, while for the CoFeB free layer structure the average critical current density was $\sim 4 \times 10^6$ A/cm^2, however it was concluded that the thermal durability of their device was not sufficient for efficient switching. Another way of reducing the critical current density is by making the free layer thinner. Albert *et al.* studied Co/Cu/Co nanopillar structures and they varied the three layers independently, thus also varying l_m in Eq. 1.1 [16]. For free layer thicknesses ranging from 1 nm-6 nm they found average critical current densities $\Delta J_C = 3.2 \pm 0.2 \times 10^7$ A/cm^2, where ΔJ_C is the difference between the critical current densities for switching of the free layer from parallel to anti-parallel alignment. From Eq. 1.1, it can be seen that a large spin-polarization results in a small critical current density. One way of reducing the critical current density is by passing unpolarized current through a half-metal. Half-metals have as the defining property that they are conducting for one spin type while being insulating for the opposite spin, i.e. they produce 100% spin-polarized currents ($\eta = 1$). Sukewage *et al.* reported a critical current density $J_C = 9.3 \times 10^6$ A/cm^2 using a multilayer consisting of an $Co_2FeAl_{0.5}Si_{0.5}$ (CFAS) alloy, which is a so-called full-Heusler alloy and a half-metal[17]. The focus of this work is in using CrO_2 to produce a spin-polarized current in a CIMS device. CrO_2 is a half-metal and can thus be used to produce a 100% spin-polarized current.

Another promising approach in realizing low dissipation devices is to utilize spintronics in combination with superconductivity. Superconductivity was first discovered in Leiden by Heike Kamerlingh Onnes in 1911[18]. At first glance it appears that superconductivity and ferromagnetism are two sections of physics which are mutually exclusive: if a strong enough magnetic field were to penetrate a superconductor, then the superconductivity would be destroyed [19] [20]. In ferromagnetic materials, the spins of the lattice align to form a macroscopic magnetic moment. In a supercurrent, the electrons condense into Cooper pairs of opposing spins. The Cooper pairs form a spin singlet system. The superconducting condensate and the ferromagnetic order are, in this sense, incompatible. However, recent developments have shown that Cooper pairs can survive in a ferromagnet if there is a magnetic inhomogeneity present between a superconductor and the ferromagnet[21]. Cooper pairs at the interface of the superconductor and the ferromagnet experiences exchange splitting, which leads to the Cooper pairs acquiring a non-zero center-of-mass momentum. The center-of-mass momentum has as a consequence that there is a mixture of Cooper pairs in the singlet configuration, and Cooper pairs in the opposing spins triplet configuration $\uparrow\downarrow + \downarrow\uparrow$. An important difference of the two spin configurations is that the singlet configuration is rotationally invariant w.r.t. the quantization axis, while the triplet configuration is not. By using another quantization axis, the $\uparrow\downarrow + \downarrow\uparrow$ configuration can be transformed into the $\uparrow\uparrow$ or $\downarrow\downarrow$ configurations. Due to spin-rotations the Cooper pairs can be in a spin triplet configuration where the spins are aligned, thus the ferromagnet does not tear the Cooper pairs apart. The combination of superconductivity and ferromagnetism can result in achieving dissipationless spintronics, specifically with the help of a spin triplet supercurrent [21][22]. It should be noted that while the evidence of the existence triplet superconductivity is clear, it still has not been shown whether the triplet supercurrent is spin-polarized. One way of characterizing the spin-polarization is with spin-transfer torque experiments[23]. One advantage of CrO_2 is the fact that the critical current density for CIMS in a CrO_2 device can be the same order of magnitude as I_C, the critical current of a CrO_2 based Josephson junction[24]. CrO_2 is thus a promising material for dissipationless spintronics applications.

Chapter 2

Theory

This chapter is concerned with the theoretical aspects of current-induced magnetization switching (CIMS). First, however, we need to consider the origin of ferromagnetism as well as the interaction between the magnetic layers. Some materials exhibit peculiar behaviour when exposed to an external magnet field **B**: they can become magnetized themselves and have their magnetization either parallel (paramagnets) or antiparallel (diamagnets) with respect to **B**. Ferromagnets are materials that retain their magnetization even after the removal of an external magnetic field, they are said to have *spontaneous magnetization* [25]. The spontaneous magnetization originates from the exchange interaction.

2.1 Ferromagnetism

2.1.1 Exchange Interaction

The exchange interaction is a purely quantum mechanical effect which has its origins in the symmetrization requirements for many-body systems of identical particles, be it bosons or fermions[26]. It is important to note that the mechanisms important for the rise of magnetism are the electron's spin, the electron kinetic (delocalization) energy, the Pauli exclusion principle, and the Coulomb repulsion between electrons [27]. For convenience, a system of two electrons will be used to demonstrate the effects of the exchange interaction. Since electrons are fermions , the sys-

tem must have a total wavefunction which is antisymmetric with respect to permutations of the electron labels, i.e.

$$\Psi(1,2) = -\Psi(2,1) \tag{2.1}$$

The total wavefunction consists of a spatial part $\psi^{S,A}$, and a spin part $\chi^{S,A}$, where the superscripts denote Antisymmetrical/Symmetrical wavefunctions w.r.t. exchange of the electron labels. It is important that the *product* of the spatial and spin part produces an antisymmetric wavefunction:

$$\Psi_- = \psi_A \chi_S \tag{2.2}$$
$$\Psi_+ = \psi_S \chi_a \tag{2.3}$$

For a system of two 1/2-spin particles the total spin S can be either S =1 with M_S = 1, 0, -1, or S = 0 with M_S = 0. The three symmetric triplet S = 1 functions are for electron 1 and 2

$$|\uparrow_1\uparrow_2\rangle \tag{2.4}$$
$$\frac{1}{\sqrt{2}}\{|\uparrow_1\downarrow_2\rangle + |\downarrow_1\uparrow_2\rangle\} \tag{2.5}$$
$$|\downarrow_1\downarrow_2\rangle \tag{2.6}$$
$$\tag{2.7}$$

and the antisymmetric singlet S = 0 function is

$$\frac{1}{\sqrt{2}}\{|\uparrow_1\downarrow_2\rangle - |\downarrow_1\uparrow_2\rangle\} \tag{2.8}$$

With $\uparrow_i$, $\downarrow_i$ denoting m_s = 1/2 and m_s = -1/2, respectively. The spatial wavefunctions can be constructed by a linear combination of the individual wavefunctions of electron 1 and 2 which are solutions of their individual Schrödinger equations,

$$\phi_S(\mathbf{r}_1,\mathbf{r}_2) = \frac{1}{\sqrt{2}}\{\psi_1(\mathbf{r}_1)\psi_2(\mathbf{r}_2) + \psi_2(\mathbf{r}_1)\psi_1(\mathbf{r}_2)\} \tag{2.9}$$
$$\phi_A(\mathbf{r}_1,\mathbf{r}_2) = \frac{1}{\sqrt{2}}\{\,\psi_1(\mathbf{r}_1)\psi_2(\mathbf{r}_2) - \psi_2(\mathbf{r}_1)\psi_1(\mathbf{r}_2)\} \tag{2.10}$$

Version of June 8, 2016– Created June 8, 2016 - 11:27

The energy of the two states (omitting spin for the moment) is found by the usual prescription $\mathcal{H}(\mathbf{r}_1, \mathbf{r}_2)\ \Psi(\mathbf{r}_1, \mathbf{r}_2) = \epsilon\Psi(\mathbf{r}_1, \mathbf{r}_2)$, where $\mathcal{H}(\mathbf{r}_1, \mathbf{r}_2)$ is the Hamiltonian of the system,

$$\epsilon_{\pm} = \int \phi^*_{S,A}(\mathbf{r}_1, \mathbf{r}_2)\mathcal{H}(\mathbf{r}_1, \mathbf{r}_2)\phi_{S,A}(\mathbf{r}_1, \mathbf{r}_2)d^3\mathbf{r}_1 d^3\mathbf{r}_2 \tag{2.11}$$

The goal of all these formalities is in acquiring the energies associated with the Coulomb interaction and quantum statistics. The energy of the system is $\epsilon_{\pm} = \mathcal{C} \pm \mathcal{J}$, where

$$\mathcal{C} = \int \psi^*_1(\mathbf{r}_1)\psi^*_2(\mathbf{r}_2)\mathcal{H}(\mathbf{r}_1, \mathbf{r}_2)\psi_1(\mathbf{r}_1)\psi_2(\mathbf{r}_2)d^3\mathbf{r}_1 d^3\mathbf{r}_2 \tag{2.12}$$

$$\mathcal{J} = \int \psi^*_1(\mathbf{r}_2)\psi^*_2(\mathbf{r}_1)\mathcal{H}(\mathbf{r}_1, \mathbf{r}_2)\psi_1(\mathbf{r}_1)\psi_2(\mathbf{r}_2)d^3\mathbf{r}_1 d^3\mathbf{r}_2 \tag{2.13}$$

$\mathcal{C}$ is called the direct, or Coulomb integral and it represents the effect the Coulomb repulsion has on the energy, or in other words, the overlap between the wavefunctions of the electrons. $\mathcal{J}$ is called the exchange integral and is a consequence of the fermionic or bosonic nature of the system of interest. In the case of the hydrogen molecule $\mathcal{J}$ is always negative, and as a consequence the singlet state is the one with lower energy. A Hamiltonian that only considers the spin functions of pairs of electrons can be used as a simple starting model for ferromagnetism. Setting the exchange integral equal to $\mathcal{J} = (\epsilon_+ - \epsilon_-)/2$, the energy can be written in the form

$$\epsilon = -2(\mathcal{J}/\hbar^2)\mathbf{s}_1 \cdot \mathbf{s}_2 \tag{2.14}$$

Eq. (2.14) can be generalized for multiple electrons on adjacent atoms and is given by the Heisenberg Hamiltonian

$$\mathcal{H} = -2\mathcal{J}\mathbf{S}_1 \cdot \mathbf{S}_2 \tag{2.15}$$

where $\hbar$ has been absorbed into $\mathcal{J}$, and $\mathbf{S}_1$, $\mathbf{S}_2$ are the total spin moments on atom 1 and atom 2, respectively. The sign of the exchange integral is important in determining the interaction of interest. $\mathcal{J} > 0$ tends to align the spins parallel w.r.t. each other and is thus a *ferromagnetic* interaction, while $\mathcal{J} < 0$ tends to align two spins antiparallel and is thus an *antiferromagnetic* interaction. Eq. 2.15 can be generalized for a lattice with pairs of electrons on site i, j

$$\mathcal{H} = -2\sum_{i,j} \mathcal{J}_{i,j}\, \mathbf{S}_i \cdot \mathbf{S}_j \tag{2.16}$$

If only nearest-neighbour interactions are taken into account, then $\mathcal{J}_{i,j}$ is a constant and can be taken outside of the summation. Unlike in a bond, the exchange interaction of a pair of electrons for free electrons is positive. The spatial part of the wavefunction with the same spin must be antisymmetric. The result of this antisymmetric spatial distribution is that no two electrons with the same spin can occupy the same place. The ion core is not screened by electrons with the same spin, leading to a reduction in the energy of the like-spin electrons: the formation of a symmetric spin state by aligning the spins with respect to each other reduces the Coulomb repulsion. The energy is reduced even further as the percentage of like-spin electrons is increased . The Heisenberg Hamiltonian is the starting point when considering theories of magnetism concerning pairwise coupling between electrons. However, the Heisenberg Hamiltonian is not sufficient for $3d$ metals Ni, Co, and Fe. Mean field theories can be used to take into account the collective exchange interactions [28] in a lattice, while band magnetism theories can be used to understand delocalised electrons. Band magnetism is the main subject of the next section.

2.1.2 Band Magnetism

Electronic band structure theory describes the properties (cohesive energy, lattice parameters, etc) of electrons in a solid [30]. For non-magnetic materials the density of states (DOS) for spin-up and spin-down electrons

Version of June 8, 2016– Created June 8, 2016 - 11:27

are the same and are thus lumped into one equation. The situation is quite different for ferromagnetic materials. The DOS for spin-up and spin-down electrons are not the same in the sense that the proportion of the DOS for one spin crosses the Fermi level more than the DOS for the other spin. The model presented here is the Stoner Wohlfarth model for the existence of ferromagnetism[28]. The energy for the two different spins is given by the ansatz

$$E_{\uparrow}(\mathbf{k}) = E(\mathbf{k}) - In_{\uparrow}/N \tag{2.17}$$
$$E_{\downarrow}(\mathbf{k}) = E(\mathbf{k}) - In_{\downarrow}/N \tag{2.18}$$

where $E_{(}\mathbf{k})$ are the energies in a normal one-electron bandstructure, $n_{\uparrow}$ and $n_{\downarrow}$ are the number of electrons with corresponding spin, and N is the number of atoms. The energy reduction due to the electron correlation is given by the Stoner parameter I. The excess of a spin type can be written as

$$R = \frac{n_{\uparrow} - n_{\downarrow}}{N} \tag{2.19}$$

The energy relations can be rewritten as

$$E_{\uparrow}(\mathbf{k}) = \tilde{E}(\mathbf{k}) - In_{\uparrow}/N \tag{2.20}$$
$$E_{\downarrow}(\mathbf{k}) = \tilde{E}(\mathbf{k}) - In_{\downarrow}/N \tag{2.21}$$

with $\tilde{E}(\mathbf{k}) = E(\mathbf{k}) - I(n_{\uparrow} + n_{\downarrow})/2N$. The occupation number is given by

$$n_i = \sum_{\mathbf{k}} f_i(\mathbf{k}) \tag{2.22}$$

where i takes into account the spin-up and spin-down states and

$$f_i(\mathbf{k}) = \frac{1}{e^{\tilde{E}(\mathbf{k}-IR/2-E_f)} + 1} \tag{2.23}$$

is the Fermi-Dirac distribution. The condition for ferromagnetism $R > 0$, is a self-consistent equation. Expanding the Fermi-Dirac functions for small R yields a condition for ferromagnetism

$$-1 - \frac{I}{N}\sum_{\mathbf{k}} \frac{\partial f(\mathbf{k})}{\partial \tilde{E}(\mathbf{k})} > 0 \tag{2.24}$$

For simplicity, the ferromagnetic condition will be evaluated at zero temperature $T = 0$. The summation over $\mathbf{k}$ becomes

$$\begin{aligned} -\frac{1}{N}\sum_{\mathbf{k}} \frac{\partial f(\mathbf{k})}{\partial \tilde{E}(\mathbf{k})} &= \frac{V}{(2\pi)^3 N}\int d\mathbf{k}(-\frac{\partial f}{\partial \tilde{E}}) \\ &= \frac{V}{(2\pi)^3 N}\int d\mathbf{k}\delta(\tilde{E} - E_F) = \frac{V}{2N}D(E_F) \end{aligned} \tag{2.25}$$

The Stoner criterion for ferromagnetism becomes

$$\frac{IV}{2N}D(E_F) > 1 \tag{2.26}$$

For elements such as Fe, Co, and Ni the theory correctly predicts their ferromagnetic existence. For materials of the 4d series the density of states and the Stoner parameter are too small to explain the existence of ferromagnetism. The theory needs to be modified and new techniques are needed. Hartree-Fock theory or self-consistent renormalisation theory of spin fluctuations give an accurate account of ferromagnetism[31].

2.1.3 Spin-Polarized Currents

The theory of itinerant electron magnetism describes the magnetic properties of delocalized electrons in a quantum mechanical fashion. The type of electrical currents of interest for this work are currents that are sent through a magnetic material and become spin-polarized. The interaction between the magnetic moments of the electrons of the solid and of the delocalized electrons results in the alignment of the spins of the electrical current. The spin current $\mathbf{Q}$ is a tensor product of the spin $\mathbf{s}$ and velocity vectors. It can be written down as[40]

$$\mathbf{Q} = \left(\frac{\hbar}{2}\right)\eta \mathbf{s} \otimes \mathbf{j} \tag{2.27}$$

Version of June 8, 2016– Created June 8, 2016 - 11:27

where **j** is the number current, $\hbar$ is the reduced Planck's constant, and η is the scalar polarization. The spin-polarization η of an electrical current is given by the difference between the spin-up and spin-down states divided by the total amount of electrons in the current

$$\eta = \frac{N_{\uparrow}(E_F) - N_{\downarrow}(E_F)}{N_{\uparrow}(E_F) + N_{\downarrow}(E_F)} \tag{2.28}$$

where E_F is the Fermi energy, and N_i are the spin-dependent density of states. The spin-polarization comes from the exchange interaction between the itinerant electrons and the magnetic moment of the atoms in the ferromagnetic material[35] [39]. If the intra-atomic exchange energy and the bandwidth for conduction electrons are comparable, then conduction electrons can be 'localized' on the atoms, which leads to the alignment of the spins of the conduction electrons. In this sense, the magnetic moment of the atoms seems to be perpetuated by the conduction electrons. In the case of half-metallic CrO_2, a current sent through the material will become 100% spin-polarized. The spin-polarization is important in inducing spin torque in a ferromagnetic layer.

2.1.4 Chromium Dioxide

A special type of ferromagnet is CrO_2 which has a half-metallic nature: it has a conduction band for one spin type, while it is insulating for the othe. Predictions [32][33][34], and experiments [36] [37] [38] have confirmed that CrO_2 is a half-metallic ferromagnet. CrO_2 has two formula CrO_2 molecules in its unit cell and crystallises in the rutile structure with space group D_{4h}^{14} [32] [33]. It has lattice parameters a = 0.4421 nm and c = 0.2917 nm. In normal ferromagnets the distinction between majority electrons (the spins that are aligned parallel w.r.t. the majority spins) and the minority electrons is useful in determining the spin-polarization of the ferromagnet of interest. The difference in half-metallic ferromagnets and normal ferromagnets is due their band properties. Co and Ni both have fully spin-polarized d-bands with a filled spin-up 3d band at the Fermi level. However, the unpolarized 4s bands also cross the Fermi level, which leads to the presence of spin-up and spin-down electron densities. The 4s band electrons impede the formation of half-metallicity. CrO_2 achieves this by hybridization of the 3d and 4s bands. An electronic band structure calculation can be seen in Figure 2.1[34]. The Fermi level E_F is set at zero.

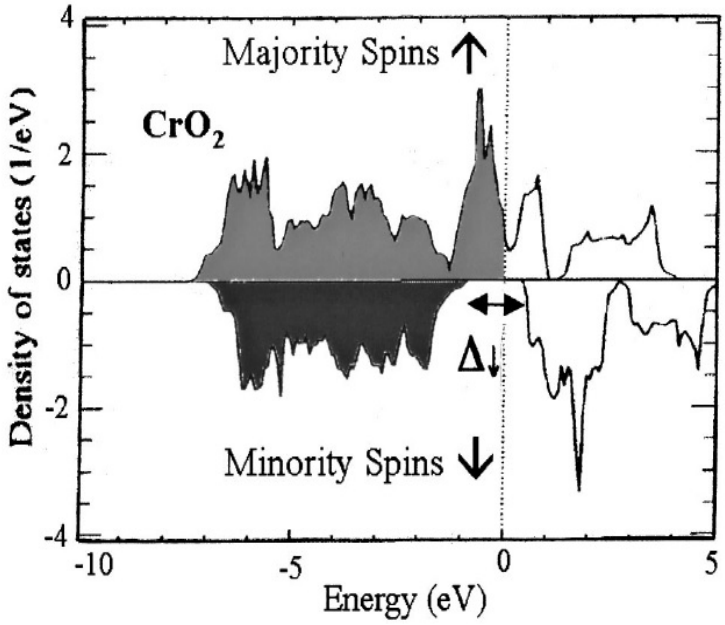

Figure 2.1: *Density of states of CrO_2 taken from ref [34]*

Due to hybridization the bottom of the 4s band is pushed above the Fermi level, and is called a type I_A half-metal. CrO_2 is a type I_A half-metal which has spin-up electrons of mainly Cr(t_{2g}) character at E_F[33]. The electronic structure consists of two low-lying O (2s) bands. The exchange split Cr (3d) states interact with O (2p) states resulting in bonding and anti-bonding states. The O (2p) and Cr (3d) states are close in energy for the spin-up electrons, and leads to a relatively strong 'covalent' interaction. For the spin-down electrons these states are far apart in energy which leads to a gap. The gap in the spin-down bands $\Delta_\downarrow > 1$eV. There is also a smaller spin-flip gap Δ_{sf} a few tenths of eV, which is responsible for spin-flip excitations at the Fermi level[33].

2.2 Magnetostatics

2.2.1 Magnetic Moment

It is known from classical physics that a moving charge distribution generates a magnetic moment, and the distribution of the magnetic moment

can be used to calculate the magnetic field generated. Similarly, there is a magnetic moment associated with the electron due to its orbital, or spin angular momentum. This section considers the macroscopic magnetic features. Simply stated, the magnetization of a body is the result of the alignment of the magnetic moments of its constituents. Magnetization can be defined as

$$\mathbf{M} \equiv \textit{magnetic dipole moment per unit volume} \tag{2.29}$$

More precisely, the magnetization is a *mesoscopic average* over time and space. Unless otherwise stated, in this section a 'magnet' is a macroscopic magnetized object.

2.2.2 The Auxiliary Field

In order to describe the magnetization of a material, an auxiliary field is needed, usually denoted as **H**. In free space the relation between the primary field **B** and **H** is $\mathbf{B} = \mu_0\mathbf{H}$. From Ampère's law it is follows that a magnetic moment is equivalent to a loop current. In a magnetic material there are two contributions to the total current density. One contribution comes from conduction currents, or free currents $\mathbf{j}_f$. The other contribution comes from 'bound' currents, $\mathbf{j}_b$, of the magnetic material.

$$\mathbf{j}_{tot} = \mathbf{j}_f + \mathbf{j}_b \tag{2.30}$$

The relation between the bound currents and the magnetization is[25]

$$\mathbf{j}_b = \nabla \times \mathbf{M} \tag{2.31}$$

Ampère's law relates the curl of the primary field **B** with the total current density, and so Ampère's law can be cast in the following form

$$\nabla \times \left(\frac{1}{\mu_0}\mathbf{B} - \mathbf{M}\right) = \mathbf{j}_f \tag{2.32}$$

The quantity in parentheses on the left hand side is the auxiliary field **H**

$$\mathbf{H} = \frac{1}{\mu_0}\mathbf{B} - \mathbf{M} \tag{2.33}$$

Converting Eq. 2.33 into a loop integral elucidates the auxiliary field's importance in determining the free currents in a magnetized object through the Ampèrian loop, namely

$$\oint \mathbf{H} \cdot d\mathbf{l} = I_{f_{enc}} \tag{2.34}$$

where $I_{f_{enc}}$ is the total free current passing through the loop.

2.2.3 The Demagnetizing Field

In the previous section **H** was defined for one macroscopic magnetic moment. Similarly, in a system consisting of several individual magnetic moments, an auxiliary field can be defined for each moment, and the total **H** is the sum of the individual moments. Each field has a contribution due to the conduction currents of the magnets $\mathbf{H}_c$ and a field due to the magnetization distribution of all the magnets $\mathbf{H}_d$. The total field $\mathbf{H}_{tot}$ can thus be split into two terms

$$\mathbf{H}_{tot} = \mathbf{H}_c + \mathbf{H}_d \tag{2.35}$$

where $\mathbf{H}_d$ is the demagnetizing field inside a magnet or as the stray field outside a magnet. We will focus on $\mathbf{H}_d$ for the moment. As was mentioned above, **H** and **B** are indistinguishable in free space, apart from the constant μ_0. However, inside a magnetic material $\mathbf{H}_d$ has an opposite orientation w.r.t. **B** and **M**, hence the name demagnetizing field. To understand the distinction of $\mathbf{H}_d$ inside and outside a magnet, the magnetostatic boundary conditions of $\mathbf{H}_d$ need to be examined. From Maxwell's equation $\nabla \cdot \mathbf{B} = 0$, it follows that $\nabla \cdot \mathbf{H}_d = -\nabla \cdot \mathbf{M}$. The boundary conditions can be found by forming a Gaussian pillbox at the boundary of the magnet. For the normal component to the surface, the boundary conditions are [25] [29].

$$H_{outside} - H_{inside} = -(M_{inside} - M_{outside}) \tag{2.36}$$

When the normal component of the magnetization across a boundary is discontinuous, the boundary conditions in Eq. 2.36 thus serve to create a field $\mathbf{H}'$. The spontaneously created field $\mathbf{H}'$ suppresses the magnetization inside the magnet.

2.2.4 Shape Anisotropy

Uniform magnetization over a body is assumed for theoretical simplicity, and is not generally valid. Uniform magnetization of a material is possible if it has an ellipsoidal shape. The demagnetizing field is given by

$$H_{di} = -\mathcal{N}_{i,j} M_j \quad i,j = x,y,z \tag{2.37}$$

where $\mathcal{N}_{i,j}$ is the demagnetizing tensor, and is a measure for the anisotropy of the system. The preference for alignment along a specific direction, in this case, is purely a geometrical consequence of the material in question. For an ellipsoid the demagnetizing tensor is just a proportionality constant. The direction of the magnetization is due to the combination of the magnetocrystalline anisotropy (discussed below) and the shape anisotropy.

2.3 Energy & dynamics

Section 2.2 dealt with the macroscopic magnetic behaviour. Here the focus is on the mesoscopic aspects of ferromagnets. The continuum approximation averages out the atomic-scale structure in favour of a magnetization $\mathbf{M}(\mathbf{r})$ which is a smoothly varying function of constant magnitude M_s, the spontaneous magnetization. We now focus on magnetic domain configurations, i.e. regions inside a ferromagnet where the magnetic moments all have the same orientation. Magnetic domain configurations are the result of minimizing the total free energy of the system. The minimum can be a local or absolute minimum in the free energy landscape. The free energy is a combination of the exchange interactions, anisotropy effects, demagnetization effects, external magnetic fields, strain and magnetostrsiction effects. The total free energy is given by the volume integral over

the sample, with the energy densities associated with the above mentioned factors:

$$E_{tot} = \int_V \left(\epsilon_{ex} + \epsilon_{ani} + \epsilon_{demag} + \epsilon_Z + \epsilon_{stress} + \epsilon_{ms}\right) dV \tag{2.38}$$

The individual terms in the integral in Eq. 2.38 are the subject of the upcoming sections.

2.3.1 Exchange Energy

The first term in Eq. 2.38 results from the quantum mechanical exchange interaction.

$$E_{ex} = \int_V \epsilon_{ex}\, dV = \int_V A(\nabla \mathbf{m})^2\, dV \tag{2.39}$$

where $\mathbf{m} = \frac{\mathbf{M}(\mathbf{r})}{M_s}$ is a unit vector in the local direction of magnetization relative to the most convenient axis of choice, usually defined by the leading term of the anisotropy(discussed below). A is the exchange stiffness, and is proportional to the exchange constant $\mathcal{J}$ in Eq. 2.16. From Eq. 2.39 it can be seen that the exchange energy is minimized when the magnetization is uniform. One important quantity to study magnetic domains is the exchange length. The exchange length is given by

$$l_{ex} = \sqrt{\frac{A}{\mu_0 M_s^2}} \tag{2.40}$$

The exchange length is a measure of the width of transitions between magnetic domains[2].

2.3.2 Magnetocrystalline Anisotropy Energy

The anisotropy energy ϵ_{ani} corresponds to the magnetocrystalline anisotropy. The anisotropy contribution is a bit more complicated expression compared to the other energy contributions as one must identify the anisotropy present in the system of interest. The crystalline anisotropy reflects the spin-orbit coupling of electrons to the crystal field. The orientation

of the magnetization relative to the crystal axes affects the magnetic energy of the ferromagnetic crystal. The *easy orientation*, or *easy axis*, is the orientation of the magnetization which minimizes the energy, only taking magnetocrystalline anisotropy into account. Two forms of magnetocrystalline anisotropy are cubic anisotropy and uniaxial anisotropy. For this work, only the uniaxial anisotropy is of importance, as this is the type of magnetocrystalline structure of CrO_2. The associated energy density is given by

$$\epsilon_{ani} = K_0 + K_1 \sin^2\theta + K_2 \sin^4\theta \tag{2.41}$$

where K_i are the anisotropy constants, and θ is the angle between the c-axis of the crystal and the magnetization. The magnetocrystalline anisotropy energy contribution is given by:

$$E_{ani} = \int_V \epsilon_{ani}\, dV \tag{2.42}$$

2.3.3 Demagnetization Energy

For convenience, assume that there is no external field. In zero field it follows that $\nabla \cdot \mathbf{H}_d = -\nabla \cdot \mathbf{M}$.

$$E_{demag} = \int_V \epsilon_{demag}\, dV = -\frac{1}{2}\int_V \mu_0 \mathbf{H}_d \cdot \mathbf{M}\, dV \tag{2.43}$$

The volume integral of a uniformly magnetized ellipsoid is zero. The demagnetizion field only has a surface contribution and is equal to the uniform demagnetizing field -$\frac{1}{2}$ μ_0 $\mathcal{N} M_s^2$, where $\mathcal{N}$ is the demagnetizing tensor.

2.3.4 Zeeman Energy

The Zeeman energy gives the energy contribution due to the interaction between the magnetization $\mathbf{M}$ and an external applied field $\mathbf{H}_a$ and is given by

$$E_Z = \int_V \epsilon_Z\, dV = -\int_V \mu_0 \mathbf{M} \cdot \mathbf{H}_a\, dV \tag{2.44}$$

The Zeeman energy is minimized when the external field and magnetization are parallel. The parallel alignment occurs only when the applied field is large enough and is thus the dominating contribution to the energy landscape.

2.3.5 Strain & Magnetostriction

Stress, like in human life, can also affect the magnetic energy of a system. It can be divided into two terms: local stress and an external applied stress. The local stress can be due to the misalignment of a magnetic material and the substrate on which it is grown and can be important for the switching behaviour of the magnetization[56]. However, for polycrystalline films strain is averaged out due to the random orientation of the magnetic domains. For CrO_2 strain does not pose a problem as it was determined that selective area growth of CrO_2 happens in a peculiar way. The growth starts at the boundaries of the selected area and forms an upward growing arch of CrO_2. The arch formation minimizes contact between the substrate and the CrO_2, reducing stress effects.

2.3.6 Magnetodynamics

Up until now the systems under consideration were assumed to be time-independent. In order to determine the magnetic behaviour in an applied field a dynamical equation is needed, which was first proposed by Landau and Lifshitz, and later expanded by Gilbert to include damping:

$$\frac{d\mathbf{M}(\mathbf{r})}{dt} = -\gamma_0[\mathbf{M}(\mathbf{r}) \times \mathbf{H}_{eff}(\mathbf{r})] + \frac{\alpha}{M_s}\left(\mathbf{M}(\mathbf{r}) \times \frac{d\mathbf{M}(\mathbf{r})}{dt}\right) \tag{2.45}$$

where γ_0 is the gyromagnetic, and α is the Gilbert damping parameter. The second term thus gives the damping and is a measure as to how quickly the field and the magnetization align, while the second term describes the precession of the magnetization around the applied field[2]. Extensions to this model will be necessary to describe spin-torque, and will be expanded upon below.

2.3.7 Magnetic Hysteresis Loops

An increasing applied magnetic field has the effect of eliminating the magnetic domains in favour of a uniform magnetization for a sufficiently large applied field. An example of a hysteresis loop can be seen in Figure 2.2.

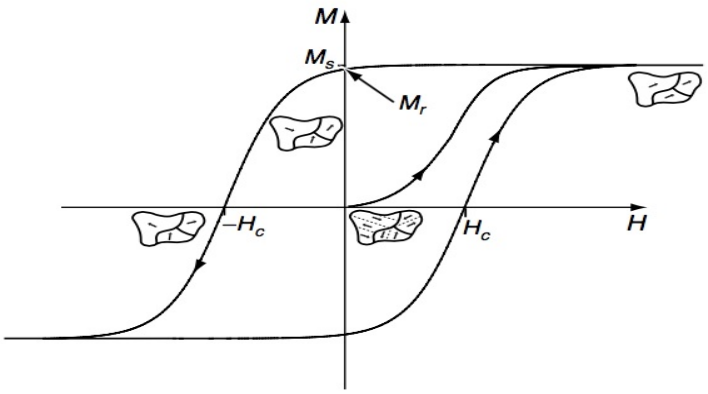

Figure 2.2: *Example hysteresis loop taken from ref [2]*

In Figure 2.2 the magnetic field is swept across one direction and the magnetization is given as a function of the applied field. Afterwards, the applied field is reversed. Reversing the field results in the formation of magnetic domains not necessarily equal to the magnetic domains prior to applying a field: hysteresis effects become prevalent. The coercive field H_C is defined as the field needed to reverse the magnetization. A hysteresis loop can give information on the strength of the magnetic body. A quite square hysteresis loop indicates a 'hard' magnet: the fact that the magnetization switches direction abruplty w.r.t. the applied field is because the magnetic body strongly prefers having a uniform magnetization.

2.4 Current Induced Magnetization Switching

2.4.1 Spin Transfer Torque & Switching

The system of interest consists of a non-magnetic metal (NM) sandwiched between two ferromagnetic (FM) layers, which will be denoted as a $FM_1/NM/FM_2$ structure. Consider the case where it is assumed that the magnetic moments of the electrons in the spin-polarized current is much smaller than the magnetization (hence magnetic moment) of the two ferromagnets: the moments of the conduction electrons do not affect the moments of the localized electrons in the ferromagnets. At the interfaces of the non-magnetic and ferromagnetic layers one needs to take into account the reflection and transmission probabilities of spin-up and spin-down electrons. For convenience, the reflection R_{min} probability for minority spins is one and for the reflection probability for majority electrons R_{maj} is zero. In Figure 2.3 the reflection and transmission of electrons is schematically shown.

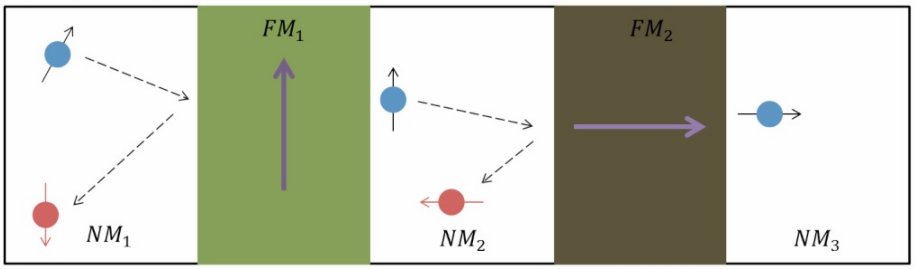

Figure 2.3: *Blue electrons belong to the majority electrons, while red electrons belong to the minority electrons. Electrons with random spin orientation in a non-magnetic metal NM_1 are incident to a ferromagnetic material FM_1. The moments of the electrons become aligned w.r.t. the magnetization $\boldsymbol{M}_1$ of FM_1 and continue to the second non-magnetic metal NM_2. When the spin-polarized electrons are incident to the second ferromagnetic layer FM_2, the transverse spin component w.r.t. the magnetization $\boldsymbol{M}_2$ of FM_2 is completely absorbed and majority electrons are transmitted. In both cases, minority electrons are primarly reflected at the ferromagnetic interfaces.*

Electrons incident from NM_1 become spin-polarized in FM_1 and travel through NM_2 to FM_2. At the second ferromagnetic layer FM_2, the incident

spin-polarized current is not collinear with $\mathbf{M}_2$. As the current traverses FM_2 the direction of the spin-polarization is changed due to alignment of the electron moments of the spin-polarized current w.r.t. the magnetization of FM_2[40]. The torque experienced by $\mathbf{M}_{1,2}$ due to the spin-polarized current is given by[12]

$$\Gamma = s\mathbf{n}_m \times \left(\mathbf{n}_s \times \mathbf{n}_m\right) = 2l_m K h_s \mathbf{n}_m \times \left(\mathbf{n}_s \times \mathbf{n}_m\right) \tag{2.46}$$

where $\mathbf{n}_m$ and $\mathbf{n}_s$ are unit vectors whose directions are that of the initial magnetization $\mathbf{M}$ and initial spin direction, respectively. $K = (1/2)MH_k$, and H_k is the uniaxial-anisotropy field, s is the spin-angular momentum deposition per unit time, and h_s is the spin-current amplitude in dimensionless units [12]. The direction of the spin-torque is determined by the orientation of the spin-polarized current, and by extension, the direction of the current density, see Eq. (2.27). In Figure 2.3 the direction of the magnetic moments are described going from left to right. The spin-torque transfer of the system in Figure 2.3 can be seen in Figure 2.4. Majority electrons from FM_1 tend to align $\mathbf{M}_2$ parallel w.r.t. $\mathbf{M}_1$, while the minority electrons from FM_2 tend to align $\mathbf{M}_1$ anti-parallel w.r.t. $\mathbf{M}_2$. If the spin current is increased to such a value that the magnetic moment of the spin-polarized current is comparable to the magnetizations of the two ferromagnetic materials, then the magnetization of the two layers will pinwheel around each other [40] in an anti-clockwise manner. If the current was to be reversed, then the pinwheeling would be in a clockwise manner. In the scenario described above it is the *transmitted* electrons that favours parallel alignment of the layers and the *reflected* electrons that favours the anti-parallel alignment. For magnetization switching it is necessary to have a magnetic layer whose magnetization will not be affected by the spin torque, the 'fixed' layer. The magnetization of the other ferromagnetic layer is such that the spin-torque can reorient its direction, and this ferromagnetic layer is the 'free' layer. Creating a fixed layer is possible by bias-exchanging the fixed layer by placing an anti-ferromagnet adjacent to the fixed layer, by choosing a 'hard' ferromagnet for the fixed layer and a 'soft' ferromagnet for the free layer, or, if using the same material for both layers, by using different dimensions for the two layers. Once a fixed and free layer is defined, then it is possible to switch magnetization of the free layer by a spin-polarized current.

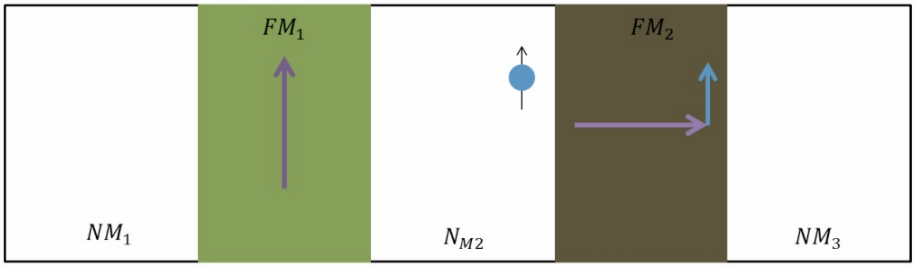

(a)

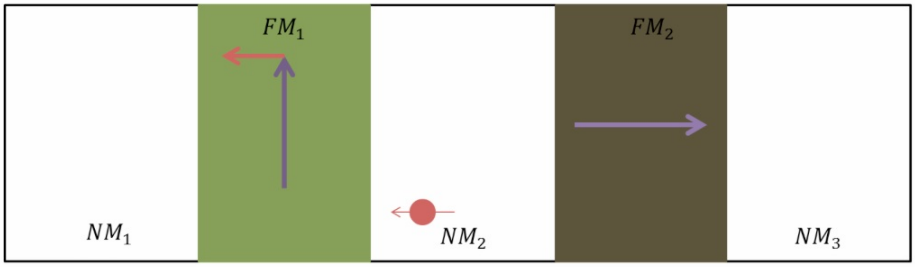

(b)

Figure 2.4: ***(a)*** *Spins from the electrons transmitted through FM_1 exert a torque on FM_2 which tends to align $\mathbf{M}_2$ parallel to $\mathbf{M}_1$.* ***(b)*** *Reflected electrons from FM_2 exert a torque on FM_1 which tends to align $\mathbf{M}_1$ anti-parallel to $\mathbf{M}_2$*

Once a fixed and free layer is defined, then it is possible to switch magnetization of the free layer by a spin-polarized current. However, the symmetry of the system is now broken due to fixing one ferromagnetic layer: it becomes important to know in which direction the current flows. Electrons transmitted from the fixed layer will cause parallel alignment of the two ferromagnetic layers. Reversing the current direction will cause reflected electrons from the fixed layer to anti-parallel align the magnetization of the two layers. The critical current density for switching, J_C, can be determined by solving the equation of motion for the spin-polarized current, and is given by [12]

$$J_C = \frac{\alpha}{\eta}\left(\frac{2e}{\hbar}\right)(l_m H_k M_s)\left(1 + \frac{2\pi M_s}{H_k} + \frac{H}{H_k}\right) \tag{2.47}$$

with α the aforementioned Gilbert damping parameter, $\mathbf{H}$ is an applied field, η is the spin-polarization of the spin current, M_s is the saturatization magnetization of the free layer, l_m is the thickness of the free layer, and e is the elementary unit charge. Typical values of the critical current density is around $\sim 10^7/\text{cm}^2$[7], such a high current density will cause destructive Joule heating in large structures. Since it is the current *density*, and not *total* current which is important for switching it is possible to reduce Joule heating by using a free layer with small dimensions. The dimensions of the free layer should, ideally, encompass a single magnetic domain. The importance of a 100% spin-polarized current becomes evident in Eq. 2.47: the critical current density can be reduced by increasing the spin-polarization. Precession of the magnetization of the free layer is a consequence of the excitations of spin waves and can also be induced by a spin-polarized current. The ground state of the ferromagnet at zero temperature is an exact solution of the Heisenberg Hamiltonian. In the ground state all spins are aligned and an excitation is thus the act of 'simply' flipping one spin. The elementary excitations of the ferromagnet look like collective modes and are called *spin waves* [30]. Going back to the exact ferromagnetic ground state, the collective modes are periodic w.r.t. the wave vector $\mathbf{q}$ of the excited spin(s). Thus, if the current density of the spin-polarized current is large enough (large $\mathbf{q}$), then it is possible to excite spin waves. The presence of spin waves result in inducing sustained magnetization oscillations in the free layer.

Chapter 3

Device Configuration

3.1 Nanopillar Criteria

We now discuss the technical details necessary for realizing CIMS. This chapter will mainly deal with the criteria for a CIMS device. Subsequently, two proposals for a CIMS device will be described. Spin-torque dynamics essentially rests on the interactions between two magnetic layers due to a current that is sent through these magnetic layers. As was discussed above, one ferromagnetic layer needs to have a fixed magnetization (fixed layer), and the magnetization of the other ferromagnetic layer (free layer) will be manipulated by the spin-polarized current. A spacer layer is placed between the two ferromagnets to decouple said layers; while the long-ranged dipole-dipole interaction is still present, the effects of the short-ranged exchange interaction between the ferromagnets is not. The thickness of the spacer layer should be much shorter than the spin diffusion length of the spacer layer, ensuring that spin-flipping processes are kept at a minimum. On top of the free layer a metallic 'capping' layer is placed. In the devices of interest, the capping layer serves to protect the underlying structures and to make electrical contact with the device. Non-trivial effects of the capping layer on the spin-torque dynamics will be discussed at the end of this chapter. A schematic representation of this 'nanopillar' device can be seen in Figure 3.1.

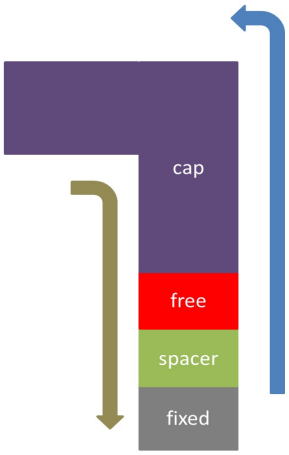

Figure 3.1: *Schematic of a nanopillar structure for current-induced magnetization switching. The current becomes spin-polarized after traversing through the fixed ferromagnet and exerts a torque on the free ferromagnetic layer. The spin-polarized current traverses through the top layer, the 'capping' layer, where electrical contact is made with the device.*

The arrows in Figure 3.1 are to remind the reader that the switching of the free layer is determined by the direction of the spin-polarized current. We are interested in abrupt switching of the magnetization of the free ferromagnetic layer. Abrupt switching is encouraged when the dimensions of the free layer are small enough to encompass a single magnetic domain. In addition, the small dimensions of the free ferromagnetic layer reduces the Joule heating of the system, compared to the Joule heating of a larger structure. However, the dimensions of the free layer should not be too small, as this would lead to superparamagnetism: the individual magnetic moments do not form a single domain and their orientation can flip randomly due to thermal excitations. As was discussed in the theory section, uniform magnetization is possible in an ellipsoidal structure [2]. For this reason, the plane of the free layer perpendicular to the current direction is a 2nm thick ellipse with a 200 nm major axis and a 120 nm minor axis. The fixed layer is much larger than the free layer and is in the shape of a bar, with the thickness in the 100nm range. The fixed magnetic layer will be the half-metallic ferromagnet CrO_2, while the the free layer will be a Ni layer. The magnetization of the CrO_2 bar is fixed by making the CrO_2 layer much bigger in all dimension w.r.t. the free layer. The long side of the CrO_2 bar is on the order of 500 μm wide, while across the bar the dimensions range in the 20 - 50 μm. With these dimensions for the CrO_2 bar it is possible to deposit multiple nanopillar structures. The nanopil-

lars are placed in the middle of the bar in order to minimize the dipole interaction. The major axis of the free layer is aligned along the long side of the bar: aligning the major axis of the free layer along the long side of the bar is favourable for abrupt switching because the magnetization of the bar prefers to align along the long side of the bar due to shape anisotropy. In addition, the long side of the bar is aligned with the magnetic easy axis of CrO_2. The consequences of shape and magnetocrystalline anisotropy were discussed in the previous chapter qualtitatively, while in the next chapter a quantitative study will be discussed. One requirement for the spacer layer is a long spin-diffusion length. One promising candidate for a non-magnetic spacer layer with a long spin-diffusion length is Cu, which has a spin-diffusion length of 350 nm at room temperature, and a spin-diffusion length of almost 1 μm at low temperatures [48] [49]. Two specific device designs are considered in this work: a 'deep' trench design, and a device design similar to the one of Andrews [46] and Özyilmaz et al. [47]. The layers in the nanopillar need to be chosen such that there is a mininum in spin-flip processes. Alongside the spin-flipping processes in the bulk of the materials, the spin-flip processes at the interfaces between materials is also important. It is essential that the interfaces are transparent for the spin current. CrO_2 is metastable and reduces to Cr_2O_3 at room temperature. The oxide layer needs to be etched before depositing any layers on top of the CrO_2, since Cr_2O_3 is antiferromagnetic and will negatively affect the spin-polarization current. In addition to the oxide layer formed on top of the CrO_2, Cu also oxidizes on its surface and requires plasma etching. Alternatively, a thin protective layer, which also *must* be transparent for the spin current, can be deposited on the Cu layer. One such spin transparent material is Ag [49].

3.2 Nanopillar Designs

3.2.1 First Nanopillar Design

The first nanopillar design consists of a thick layer of SiO_2 on top of a TiO_2 substrate. The trench is made by selective Reactive Ion Etching (RIE) of the SiO_2 layer. Selective etching is possible by lithographically defining the lateral dimensions of the trench. After development the remaning resist serves as a protective layer for the SiO_2 layer during RIE. With the help of selective area growth, CrO_2 is deposited in the trench. After growth of

the CrO_2, Cu and Ni are deposited in the trench to finish the structure. The trench fabrication and the electrical contact formation need to be done in two lithographic steps. Figure 3.2 is a schematic cross section of the first nanopillar design. The layers of Cu and Ni are deposited across the side of the trench. The fabrication of the electrical contact is not a concern for this work, as it was concluded that this step has been optimized[50]. The main concern of this work is the fabrication of the deep trench and growth of CrO_2 in the trench.

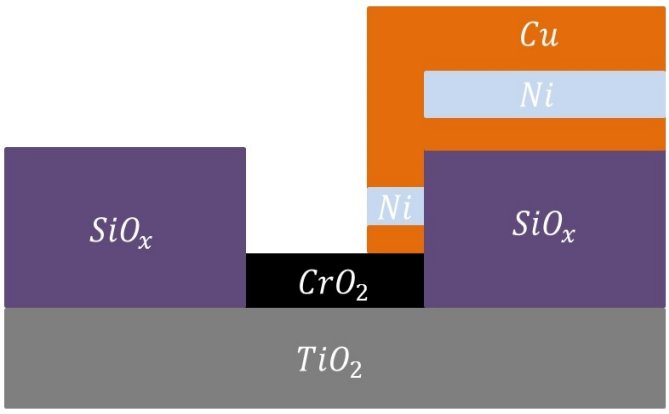

Figure 3.2: *Deep trench nanopillar design with the Cu/Ni/Cu 'fingers' on one side of the trench.*

The Cu and Ni layers inside the trench need to be discontinuous from the Cu and Ni layers on top of the SiO_x. If the Cu layers in the trench and on top of the SiO_x are connected, then efficient magnetization switching of the Ni layer will be hampered. An undercut is necessary when depositing the remaining layers: an undercut ensures that the layers in the bottom of the trench and on top of the SiO_x are discontinuous. The walls of the trench in Figure 3.2 were not designed to have an undercut. Deposition of the subsequent pillar layers does not lead to discontinuity of the Cu and Ni layers in the trench and the layers on top of the SiO_x. Figure 3.3 is a schematic cross section of the true outcome of deposition in a trench with no undercut.

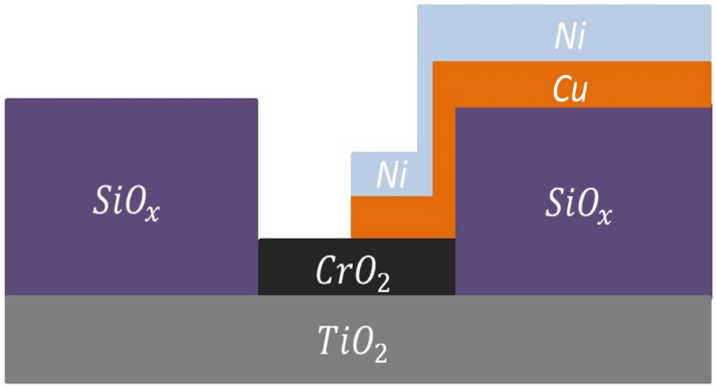

Figure 3.3: *Without an undercut, the layers of Ni and Cu would not be discontinuous. The deep trench nanopillar design does not incorporate formation of an undercut.*

3.2.2 Nanopillar design part deux

The second nanopillar design, and the main focus of this work, involves creating a hole in a nanostencil and depositing the rest of the nanopillar on top of the underlying Cu/CrO_2 layers. Figure 3.4 is a schematic cross section of the final device design. A trench is made by electron beam lithography in a 25 nm thick SiO_2 layer that is sputter-deposited on top of a TiO_2 substrate. Selective area growth of the CrO_2 layer is done by chemical vapour deposition (CVD) in the SiO_2 trench. Afterwards, a 5 nm thick Cu layer is sputter-deposited on the CrO_2. The Cu layer is structured into a 2μm by 2μm square by a lift-off procedure. The Cu layer serves two functions: it is the spacer layer for the CIMS device, and it serves as a protective layer for CrO_2 during wet-etching. After lift-off, a bilayer of SiO_2 and Pt is sputter-deposited, with the former having a thickness of 200nm and the latter being 10 nm thick. An elliptical hole is made in the Pt layer. The elliptical hole is necessary to make an elliptical free layer. The elliptical hole in the Pt mask lies above the Cu layer. To reach the Cu layer, the SiO_2 layer is etched with an aqueous solution of hydroflouric acid (HF).

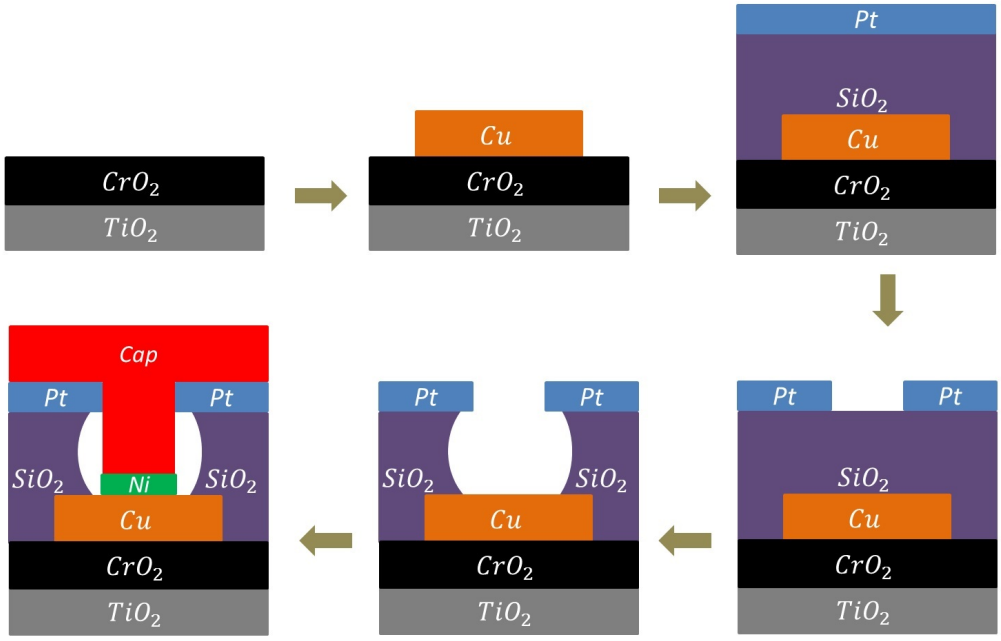

Figure 3.4: *Cross section of layered nanopillar structure, this picture needs to be altered to include the composition of the capping layer will be discussed in the chapter on fabrication.*

The Cu layer is plasma etched to get rid of the top oxide layer. After cleaning the Cu layer, a 1.5 nm thick Ni layer is sputter-deposited on the Cu. On top of the Ni layer comes the final layer(s) of a conducting metal, the so-called capping layer. The top layer is patterned again with electron beam lithography and an etching procedure is used to acquire the desired geometry for the top electrical contact. The nanopillar structure is placed in the middle of the CrO_2 bar in order to minimize the dipole interaction of the CrO_2.

3.2.3 Capping Layer

Non-trivial behaviour occurs when a capping layer is used in a CIMS structure. The primary purpose of the capping layer is to protect the underlying CIMS structure. It turns out that a capping layer also increases the spin transfer torque, thereby reducing the current needed for magnetization switching. Specifically, deposition of a capping layer with a strong

spin-relaxation (short spin-diffusion length),on top of the $FM_1/NM/FM_2$ composition described enhances the spin-torque in a non-local way. The effects of spin accumulation and the chemical potential gradient is important in understanding the enhancement of the spin-torque. Chung [44] and Kumar et al. [42], studied the effects of a capping layer in multilayer spin transfer torque structures and can be understood as follows. The transport process under consideration is a diffusive process, since it is the spin-relaxation of the capping layer which is responsible for the change in the spin transfer torque. For convenience, a one-dimensional diffusion process is considered and can be described by the one-dimensional diffusion equations for the spin-current densities [45]

$$J_{\uparrow,\downarrow} = \frac{\sigma_{\uparrow,\downarrow}}{e}\frac{\partial \mu_{\uparrow,\downarrow}}{\partial x}, \quad \frac{\Delta\mu}{\lambda^2} = \frac{\partial^2 \Delta\mu}{\partial x^2} \tag{3.1}$$

where σ_i and μ_i are the conductivity and electrochemical potentials of the different spins, respectively. The spin-polarized current density is thus $J_s = J_\uparrow - J_\downarrow$. The spin-torque experienced by the free layer is proportional to this spin-polarized current density

$$\tau_{FM2} \propto J_S \propto SI_{FM2} \tag{3.2}$$

From Eq. 3.1 it can be seen that the spin-polarization depends on the chemical potential difference between the two spin currents. Strong spin-relaxation in the capping layer has as a result that the chemical potential gradient, over the entire structure, is increased. The increase in the gradient of the chemical potential thus leads to a larger spin-polarization in the non-magnetic layer, which in turn leads to a larger spin-torque on the free layer. It can be concluded that the gradient of the chemical potential over the entire device is the cause of the excess in spin transfer torque. Yang et al. [43] carried out CIMS experiments with Co/Cu/Co structures which had either a Cu or Au as a capping layer. They observed a reduction in critical current density needed for magnetization switching for the structure with the Au capping layer as opposed to the Cu capping layer structure. The situation described above concerned the spin-polarization of currents which are not 100% spin-polarized. The capping layer serves to enhance the spin-polarization, and hence, the spin transfer torque. It remains to be seen if there is an excess torque due to the capping layer in a 100% spin-polarized current, since the polarisation cannot be further enhanced. However, in real setups the spin-polarization of even CrO_2 is

very high, but not quite 100%, which might be due to impurities in the device. In the best case, the capping layer might help in making the almost 100% spin-polarization come even closer to 100% spin-polarization. In the worst case, there might be no excess torque and the only function of the capping layer will be as its original goal of a protective layer for the underlying structure.

Chapter 4

Micromagnetic simulations

Since the 1980's an increase in computing power made it possible to study micromagnetics in an increasingly detailed fashion [51]. More powerful computers can help in the understanding of micromagnetics which in turn can lead to developing devices that can improve computing power. In order to find the optimal device configuration micromagnetic simulations were carried out with the help of the OOMMF (Object-Oriented Micro-Magnetic Framework) software package [52]. Investigations into the coercivities and effects of shape anisotropy of Ni,Co, and CrO_2, is the main focus of this chapter.

4.1 Micromagnetics and OOMMF

4.1.1 OOMMF

OOMMF is a powerful and widely used tool to investigate magnetization dynamics. OOMMF is an object oriented approach to magnetization dynamics. The object oriented approach makes it possible for a programmer to not be bogged down by the subtleties of the C++ functions used to solve a specific micromagnetic problem. Instead, the programmer can quite easily define a system to study. If it is needed for the question at hand, the C++ functions can be modified, however this does require an understanding of the subtleties of the approximation schemes used in OOMMF. OOMMF codes can be modified at 3 distinct levels.

The lowest level consists of the actual C++ source code which solves the Landau-Gilbert differential equations. The intermediate level consists of the Tcl/Tk scripts wherein the geometry and material parameters are defined. The most direct level of modification consists of individual programs that interact with each other via well-defined protocols across network sockets. OOMMF employs Fast Fourier Transforms (FFT) to compute the self-magnetostatic (demag) field [53]. Finite Element (FE) techniques ares utilized by OOMMF to solve the differential equations in magnetodynamics. The parameters used for calculations, exchange stiffness, uniaxial anisotropy, etc, are given in Table 4.1. As some calculations may never converge, two conditions are fed into OOMMF to determine when it should stop with calculating the magnetization. For each stage step, e.g. magnetic field step, a finite amount of iteration steps can be imposed. In the calculations done in this work ten thousand iteration steps is imposed. The other restriction concerns the change in magnetization direction. If the total magnetization direction changes too abruptly, then OOMMF continues calculating the total magnetization until either the change in total magnetization direction is no longer abrupt, or the maximum amount of iteration steps has been reached. The magnetization direction criteria is determined by setting a maximum value to $|\frac{d\mathbf{m}}{dt}|$, which has units of degrees per nanosecond and $\mathbf{m}$ is the unit magnetization direction. In the calculations $|\frac{d\mathbf{m}}{dt}| = 0.01$ The calculations do not take thermal effects into consideration, i.e. $T = 0$.

4.1.2 Micromagnetic computation

Micromagnetism is an approximation scheme which assumes that the magnetization is a continuous function of position, and derives relevant expressions for the important contributions arising from the exchange, magnetostatic, and anisotropy energies. Acquiring a stable equilibrium state is possible by minimizing the Gibb's free energy Eq. 2.38.

$$E_{tot} = \int_V \left(\epsilon_{ex} + \epsilon_{ani} + \epsilon_{demag} + \epsilon_Z + \epsilon_{stress} + \epsilon_{ms}\right) dV \tag{4.1}$$

When a magnetic moment $\mathbf{m}$ is placed in an external magnetic field, which is inclined to $\mathbf{m}$, the magnetic moment experiences a torque $\Gamma = \mathbf{m} \times \mathbf{B}$. The dynamics of the torque is given by the Landau-Lifshitz-Gilbert equation

Eq 4.2.

$$\frac{d\mathbf{M}(\mathbf{r})}{dt} = -\gamma_0[\mathbf{M}(\mathbf{r}) \times \mathbf{H}_{eff}(\mathbf{r})] + \frac{\alpha}{M_s}\left(\mathbf{M}(\mathbf{r}) \times \frac{d\mathbf{M}(\mathbf{r})}{dt}\right) \tag{4.2}$$

The torque tends to align **m** along the external magnetic field. As was mentioned above, FE techniques are utilized in OOMMF. The FE method is an approximation scheme used to solve partial differential equations (PDE). In solving a PDE, the FE method consists of three main steps. The FE method consists of turning a PDE problem into an algebraic problem. The domain of the PDE is discretized into finite elements. An approximation of the PDE is found by using piecewise continuous polynomials. The piecewise continuous polynomials discretizes the PDE and the system is split into a finite number of algebraic equations. The coefficients of the polynomials are determined in such a way that the distance to the exact solution of the PDE is minimized. The distance to the exact solution is defined by the norm in a suitable vector space. The finite elements refers to the many small subdomains of the solution domain. The FE mesh, or grid, is the collection of all the finite elements. The shape of the elements can be made by dividing the entire region of the FE solution into various shapes. The flexibility of the element shapes makes the FE method a powerful tool when one is dealing with complex geometries. In OOMMF the discretized finite elements are magnetic domains which are under the constraints of the Gibb's free energy and the Landau-Lifshitz-Gilbert differential equation. The Gibb's free energy and Landau-Lifshitz-Gilbert expressions are transformed into PDE by first variation w.r.t. their variables.

	CrO_2	Co	Ni
A(J/m)	4.6×10^{-12}	3.0×10^{-11}	9×10^{-12}
K_1 (J/m^3)	2.7×10^4	5.2×10^5	-5.7 $\times 10^3$
M_s (A/m)	4.75×10^5	1.4×10^6	4.9×10^5

Table 4.1: *Parameters used for the calculations: exchange stifness A, anisotropy constant K_1, and saturation magnetization M_s*

4.2 Coercivity of the magnetic fixed and free layers

4.2.1 Co and Ni as free layers

To determine the usefulness of Ni as a free layer simulations were done to determine the coercivities of a Ni ellipse and a Co ellipse. Switching should be an abrupt process, leaving no ambiguities between the ”on” state and ”off” state of the free layer. The layers of Ni and Co are thus of the same dimension, the only difference being their magnetic properties (120 nm by 200 nm by 2 nm). Ni has a cubic magnetocrystalline anisotropy. However, due to the very thin nature of the Ni layer it is not possible to define cubic anistropy axes. As a result, the Ni layer was given a random magnetization and the shape anistropy was the only contributing factor in the equilibrium magnetization of the Ni layer. However, it was concluded that the absence of the magnetocrystalline anisotropy due to the thin nature of the Ni layer does not signficantly affect the magnetization of the system [54]. Figure 4.1a and Figure 4.1b are hysteresis loops for the Co and Ni ellipses: the magnetization of the Co and Ni layers as a function of the applied external field. The layers are 2nm thick ellipses, with a minor axis of 120nm and a major axis of 200nm. The magnetic field is swept from -150 mT to 150mT (and reversed) in steps of 5mT. The mesh size for the Ni and Co calculations is 2nm by 2nm by 1nm. The Ni ellipse saturates around 10 mT, while the Co ellipse saturates around 25 mT. As was mentioned before, an abrupt switching field is necessary for the free layer. The hysteresis loops show that the Ni layer switches more abrupt than the Co layer: the Ni hysteresis loop is more ’square’ than that of Co. The hysteresis loops also show that Co is a much harder magnet than Ni. It can be concluded that Ni switches more abruptly than a Co free layer for the geometry under consideration. However, the question remains of whether this abrupt switching of the Ni layer is enough to produce a measurable signal. However, in the CIMS literature the use of Ni as a free layer is not common. Co as a free layer in CIMS is favorable due to the large acquired signal.

Version of June 8, 2016– Created June 8, 2016 - 11:27

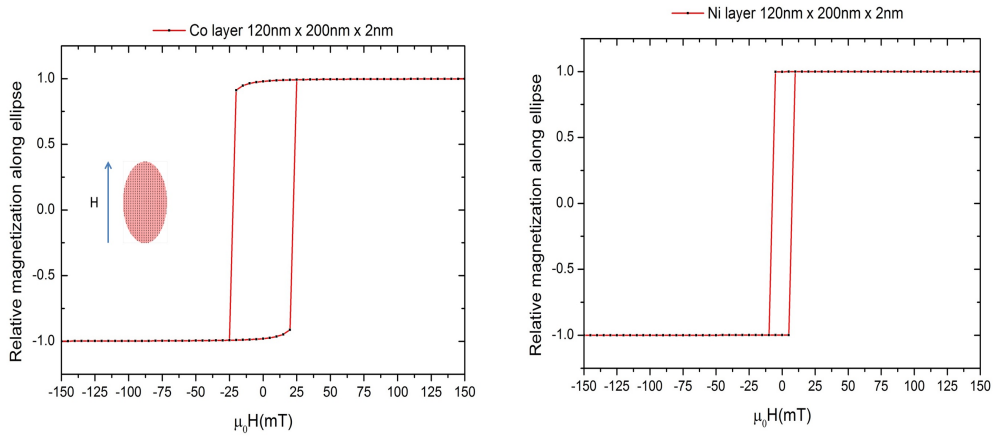

(a) ***(b)***

Figure 4.1: *Calculated hysteresis curves for* ***(a)*** *Co, and* ***(b)*** *Ni. The magnetization for Co switches at a field of 25 mT, while for Ni the magnetization switches at 10 mT. The magnetization of the Co and Ni layers are normalized, reaching a maximum/minimum of* $\pm$ *1.*

The large signal conundrum can be seen by comparing the products of the residual resistivity, ρ_0, and spin diffusion length, l_{sp}, of Ni and Co [49]. The product $\rho\ l_{sp}$ for Co is much larger than for Ni: 2.4 fΩ m^2 for Co at 4.2 K compared to 0.7 fΩ m^2 for Ni at 4.2 K. In other words, the change in resistance for Co will give a bigger signal than the change in resistance for Ni when considering $\rho\ l_{sp}$. As was mentioned above, the switching of the magnetization of the free layer should occur abruptly. Another condition concerns the switching of the magnetization of the fixed layer. The fixed layer is considered fixed in the sense that the coercivity of the fixed layer should be much larger than that of the free layer. Some questions of interest are: How is the coercivity of the fixed layer affected by its magnetocrystalline and shape anisotropies? Is it possible to optimize the fixed layer geometry in such a way that its coercive field is much larger than the coercive field of the free layer? In order to answer these questions, the hysteresis behaviour for different geometries need to be stated. The fixed layer coercivity is the topic of the next section.

4.2.2 Chromium dioxide coercivity

The magnetocrystalline anisotropy is studied by designing rectangular bars of CrO_2, with the long side of the bar either being along the magnetic easy axis, or along the magnetic hard axis. In addition to the bars, the magnetization dynamics of squares of CrO_2 are also calculated with the magnetic easy axis being in the plane of the squares. In Figure 4.2 hysteresis loops are plotted for CrO_2 magnets with the long side of the bar along the magnetic easy axis of CrO_2. In this configuration the magnetocrystalline anisotropy and the shape anisotropy of the CrO_2 cooperate in determining the magnetic state of the CrO_2. The thickness (100 nm) and length (5μm) of the bars are kept fixed. Three different widths are used to study the coercivity of the bars, namely widths of 2 μm, 500 nm, and 200 nm.

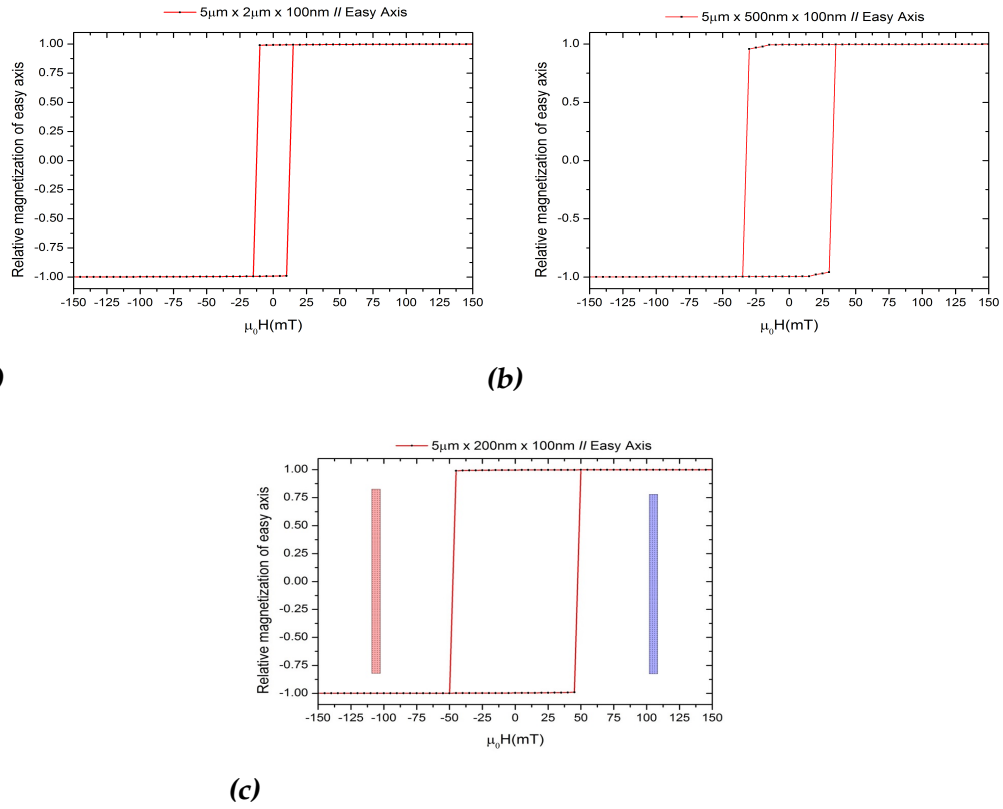

Figure 4.2: *Magnetization hysteresis loops for 100 nm thickCrO_2 bars with the long axis of the bar aligned along the magnetocrystalline easy axis, with widths of* ***(a)*** *2μm,****(b)*** *500nm,* ***(c)*** *200nm, having coercive fields 15 mT, 35 mT, and 50mT of respectively.*

The mesh size for the CrO_2 calculations is 8 nm by 8 nm by 2 nm. The magnetic field is swept from -150 mT to 150mT (and reversed) in steps of 5mT. The first observation that can be made is the square shape of the hysteresis loops. The magnetization of all three bars switch quite abruptly, however the coercivity is not the same for the different widths. A narrower width of the bar results in a larger coercive field needed to switch the magnetization. Decreasing the bar width, while keeping the other dimensions fixed, increases the shape anisotropy of the CrO_2, resulting in the magnetization favouring being strongly aligned along the long axis of the bar. Due to the magnetic easy axis being aligned along the long side of the bar, the shape and magnetocrystalline anisotropies cooperate and ensure that the switching of the magnetization is an abrupt process: it is energetically unfavourable to form magnetic domains in the bar whose magnetizations are not aligned along the bar. The coercivities of squares of CrO_2 are calculated to determine the limit where the shape anisotropy does not affect the coercivity of the CrO_2 structure. In Figure 4.3 the magnetization vs applied field hysteresis loops of the squares of CrO_2 are plotted.

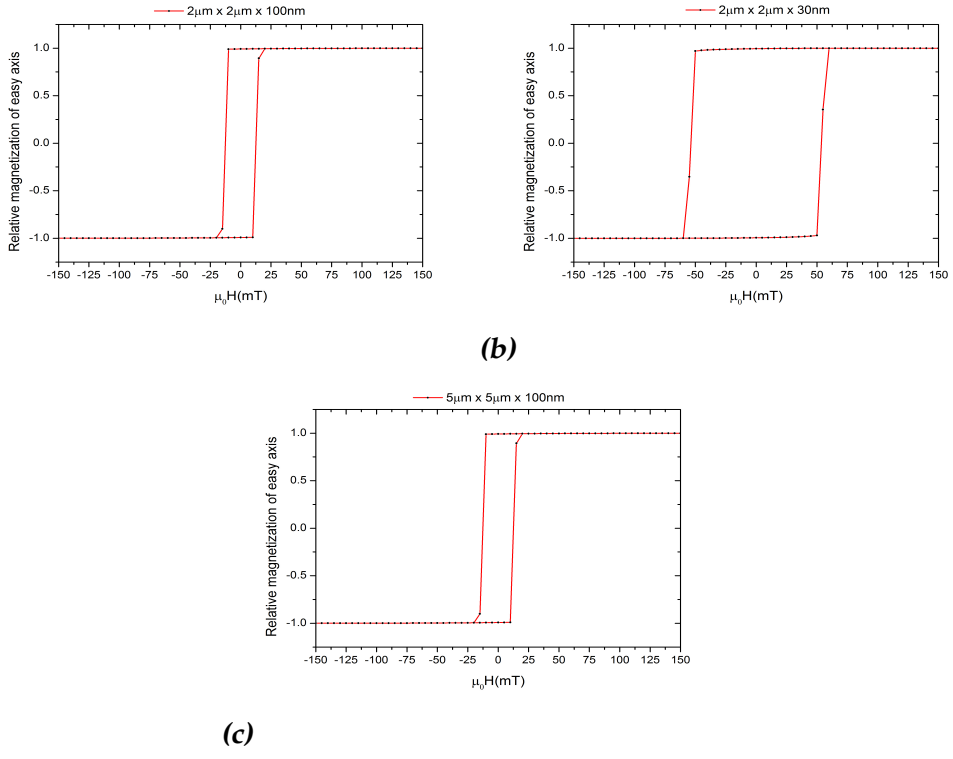

Figure 4.3: *Hysteresis loops for CrO_2 squares with the magnetic easy and hard axis in the plane of the square.*

Three different square structures are considered two 2μm by 2μm squares, one being 100 nm thick and the other being 30 nm thick, and one 5μm by 5μm square with a thickness of 100 nm. The magnetic easy and hard axes are in the plane of the squares and a magnetic field is applied in the direction of the easy axis of the squares. The magnetic reversal along the easy axis is quite abrupt. The magnetization for the 2μm by 2μm and 5μm by 5μm squares with a thickness of 100 nm behave the same: both have coercive fields of 15 mT, which indicates that increasing the size of the squares does not influence the magnetization. The hysteresis loop for the thinnest square, as shown in Figure 4.3b, requires the largest field to switch the magnetization. In the theory chapter it was discussed that magnetostriction and stress can significantly affect the magnetization. Magnetostriction in real systems of thin CrO_2 structures is important [56] [58], however this is not the case for the current calculation: the simulation does not take magnetostriction effects into account because in the calculation the CrO_2 structures are in a 'vacuum' and are essentially devoid of any magnetostriction effects due to growth processes. The harder coercivity stems from the fact that making the square thinner supresses the out-of-plane component in the magnetization, hence reducing the degree of freedom allowed for reversal.

In the start of this section the behaviour of CrO_2 bars aligned along the easy axis was studied. The next step is to study the behaviour of CrO_2 bars that are aligned along the magnetic hard axis. In Figure 4.4 the hysteresis loops for CrO_2 bars with the long side of the bar aligned along the hard axis are plotted. The magnetic reversal of the bars in Figure 4.4 is not as abrupt as the reversal of the bars in Figure 4.2, as can be seen by the shape of the hysteresis loops. The hysteresis loops in Figure 4.4 show that the magnetic dynamics of the bars are quite different than those where the bar was aligned along the magnetic easy axis. The hysteresis loop for the widest bar (2μm) shows the magnetization switches more abruptly than the narrower structures.

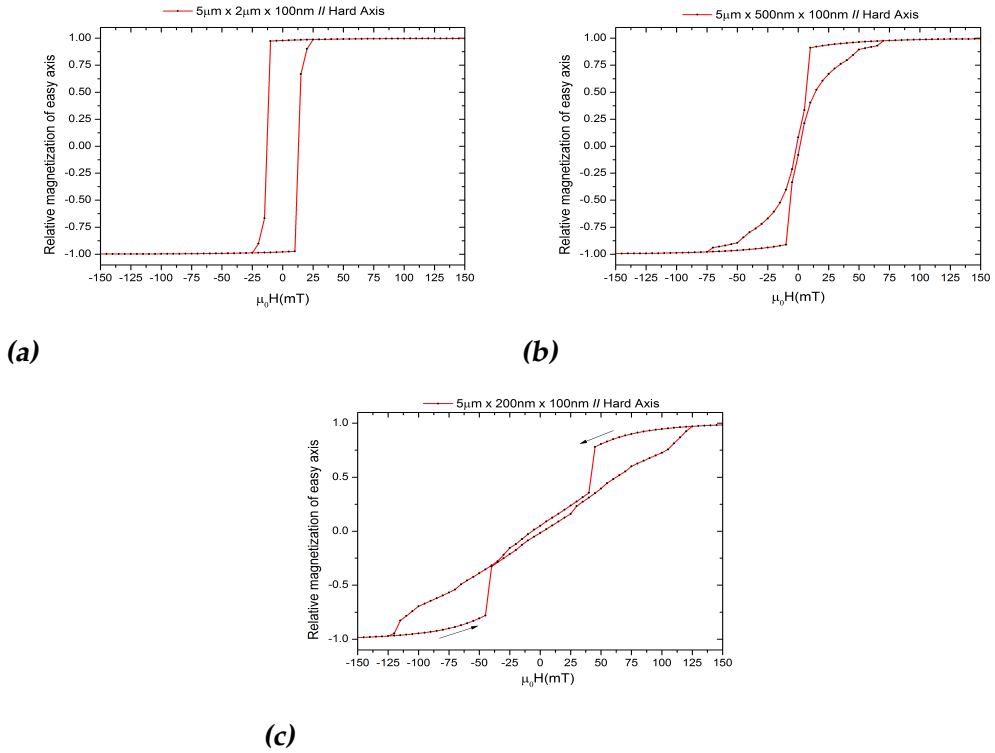

Figure 4.4: *Magnetization hysteresis loops for the CrO_2 bars with the long side of the bar aligned along the magnetic hard axis for widths of* ***(a)*** *2μm,* ***(b)*** *500 nm, and* ***(c)*** *200 nm, with coercive fields of 15 mT, 5 mT, and 5mT, respectively.*

To understand the hysteresis loops for the 500 nm and 200 nm wide bars it is useful to visualize the spatial variation of the magnetization of the bars, shown in Figure 4.5. In Figure 4.5 blue corresponds to alignment of the magnetic moments along the positive external field direction, while red corresponds to alignment along the negative field direction. White indicates an out-of-plane magnetization component. The field is applied across the bar. Bottom magnetization bars are for sweeping from negative to positive field values and vice versa for the top magnetization bars. Magnetic field strengths for the bottom three bars are, from left to right: -5 mT, 15 mT, 65 mT. Magnetic field strengths for the top three bars are, from right to left: 5 mT, -30 mT, -65 mT.

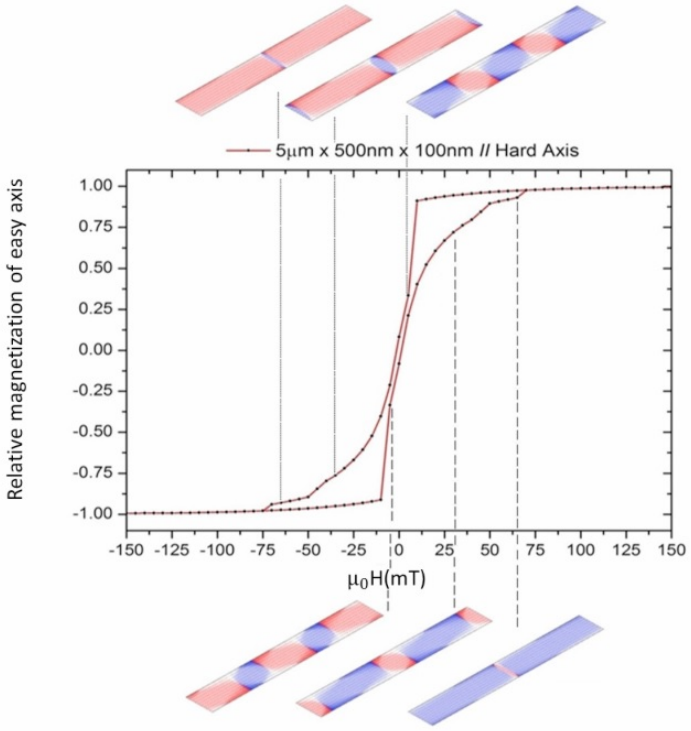

Figure 4.5: *Hysteresis loop of the 500 nm wide bar along with the magnetization of the bar.*

As is seen by Konig et al. [57], magnetic domains are seen at low applied magnetic field strength. Magnetic domains with antiparallel magnetizations w.r.t. each other are formed at low field strengths due to the competition of the shape and magnetocrystalline anisotropies. For strong external magnetic fields the magnetization is in the direction across the bar. In Figure 4.6 the magnetic hysteresis loop along with the magnetization of the 200 nm bar is shown. In Figure 4.6 blue corresponds to alignment of the magnetic moments along the positive external field direction, while red corresponds to alignment along the negative field direction. White indicates an out-of-plane magnetization component. The field is applied across the bar. Bottom magnetization bars are for sweeping from negative to positive field values and vice versa for the top magnetization bars. Magnetic field strengths for the bottom three bars are, from left to right: -45 mT, 0 mT, 100 mT. Magnetic field strengths for the top three bars are, from right to left: 45 mT, 0 mT, -100 mT.

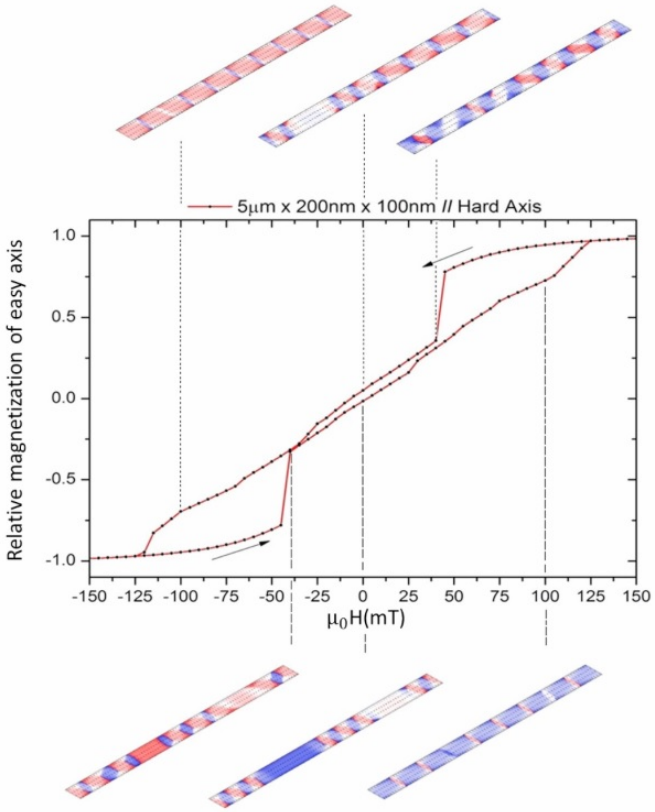

Figure 4.6: *Hysteresis loop of the 200 nm wide bar along with the magnetization of the bar along with a visualization of the micromagnetic configuration.*

At low external field strengths the contribution to the magnetization due to shape anisotropy begins to take effect: shape anisotropy favours alignment of the magnetization along the bar. Due to the strong magnetocrystalline anisotropy the shape anisotropy does not dominate, instead domain vortices are formed. At zero field there is also a strong out-of-plane magnetization component for both sweep directions, however the magnetizations at zero field for the two sweeping directions are not exactly the same. The slight asymmetry is due to the fact that at zero field the system is in a metastable state. As was mentioned above, the calculations were carried at $T = 0$. In real systems, the nucleation of domains at zero field is due to thermal excitations. Figure 4.6 also shows that there are more magnetic domains formed in the 200 nm bar compared to the 500 nm hard bar. One important difference between the 200 nm wide bar and the 500 nm wide bar is the form of the magnetic domains, which is shown in Figure 4.7. In the 500 nm wide bar the magnetic domains are arranged in a stripe

pattern: the magnetization of adjacent domains are antiparallel w.r.t. each other. In the 200 nm wide bar the magnetic domains form vortices.

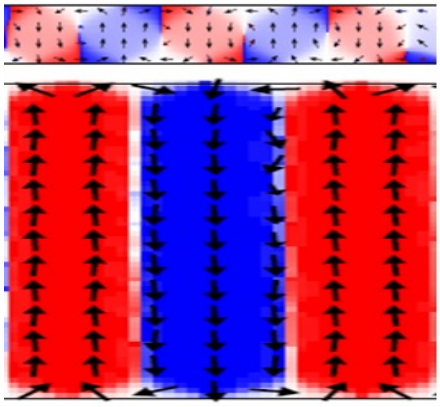

Figure 4.7: *Magnetic domain configuration at zero magnetic field of CrO_2 bars with long axis along magnetic hard axis of* ***top****: 200nm wide bar,* ***bottom****: 2μm wide bar (not to scale).*

The width d of a domain wall at equilibrium is given by [59] [60]

$$d = L\sqrt{\frac{\sigma_D}{1.7\mu_0 M_s^2 t}} \tag{4.3}$$

with t the thickness of the bar, M_s is the saturation magnetization, μ_0 the permeability in free space, L is the width of the bar and σ_D is the domain wall energy density. The domain wall energy density can be approximated by

$$\sigma_D \sim \sqrt{AK_\mu} \tag{4.4}$$

where A is the exchange stiffness, and K_μ is the uniaxial anisotropy constant. Using the values in Table 4.1, the width of the domain walls is calculated to be d = 42.7 nm. For the 500 nm wide bar the average domain wall width is 36.5 nm $\pm$ 4.0 nm, being in reasonable agreement with Eq. 4.3 using the approximation in Eq. 4.4. However, Eq. 4.4 is not valid for vortices, and is reflected in the simulations where the calculated width is 17.1 nm, and the average width of the domain walls in the 200 nm hard bar at zero field is 28.7 nm $\pm$ 2.5 nm. The formation of vortices also has

a direct consequence on the reversal mechanism as can be seen by comparing the hysteresis loops of the 200 nm wide bar. In the work of Kronig et. al. [57] CrO_2 nanowires were fabricated with widths in the 0.5 μm - 5.0 μ range, having a thickness of approximately 60 nm. The long side of the bars were in the 100 μm range. The long side of the CrO_2 bars were aligned parallel to the magnetic easy axis, orthogonal to the easy axis, or with directions of the long axis that were in between the parallel or orthogonal orientations. For bars aligned along the hard axis they reported striped domain structures similar to the one in the 500 nm hard bar in the simulations presented here. However, they did not report observing vortex magnetic domains. The vortices and hysteresis loops for the 200 nm wide nanowires can also be seen in calculations of Boardman [55]. In his work, Boardman calculated the hysteresis loops and micromagnetic configurations with OOMMF of various Ni structures (nanodots, spheres, half-spheres, and cylinders) and conical permalloy structures. The calculations on different geometries all had a similar behaviour when the dimensions of the system is increased and as the applied field is varied. Single domain configurations in the various structures are observed for large applied fields. As the field is reduced the dimensions of the structures begin to have an effect on the magnetization: as the dimensions of a structure is increased, the magnetization switches from a single domain configuration into a vortex state. The vortex state is due to the growing dipolar contribution which accompanies the increase in size of the structure dimensions. In the case of the 200 nm wide bar, the width of the bar is of the same order as the structures in Boardman's calculations. The long axis of the bar makes it possible to form multiple vortex domains. However, in Boardman's calculations they focused on the effects of shape anisotropy of their structures, which were either spheres, dots or conical structures, and not on the magnetocrystallinity. The vortices in Boardman's structures are a consequence of minimizing the shape anisotropy contribution to the free energy. In our calculations the vortices are due to the competition of the shape and magnetocrystalline anisotropies of the CrO_2 bar. In Table 4.2 the dimensions of the CrO_2 bars are given, along with the orientation of the long side of the bar and the corresponding coercive fields.

CrO_2 bar dimension	$\mu_0\ H_{coerc}$ (hard)	$\mu_0\ H_{coerc}$ (easy)
200 nm $\times$ 5 μm $\times$ 100 nm	5 mT	50 mT
500 nm $\times$ 5 μm $\times$ 100 nm	5 mT	35 mT
2μm $\times$ 5μm $\times$ 100 nm	15 mT	15 mT

Table 4.2: *Dimensions of the CrO_2 bars and their corresponding coercive fields*

CrO_2 square dimension	$\mu_0 H_{coerc}$
2μm $\times$ 2 μm $\times$ 30 nm	55 mT
2μm $\times$ 2 μm $\times$ 100 nm	15 mT
5μm $\times$ 5μm $\times$ 100 nm	15 mT

Table 4.3: *Dimensions of the CrO_2 squares and their corresponding coercive fields*

4.2.3 Spin-transfer torque

OOMMF also offers an experimental solver package which takes into account spin-transfer torque effects, which is mentioned here for completeness. The effects of spin-transfer torque can be modeled by adding a spin momentum term to the Landau-Lifshitz-Gilbert differential equations:

$$\frac{d\mathbf{m}}{dt} = -|\gamma|\mathbf{m}\times\mathbf{H}_{eff} + \alpha\left(\mathbf{m}\times\frac{d\mathbf{m}}{dt}\right) \tag{4.5}$$

$$+|\gamma|\beta\epsilon(\mathbf{m}\times\mathbf{m}_p\times\mathbf{m}) - |\gamma|\beta\epsilon'\mathbf{m}\times\mathbf{m}_p \tag{4.6}$$

The spin-torque evolver does not take temperature effects into account, i.e. T = 0. The spin-torque evolver can be used for CIMS, however the method is still underdeveloped so future work on the package is needed before it can be used to give accurate results.

4.2.4 Conclusion

The calculations of Ni, Co and CrO_2 structures reveal that a CrO_2/Ni CIMS device would be ideal for abrupt switching of the free Ni layer. However a CrO_2/Co CIMS structure would give a larger signal, due to the higher resistivity area product of Co compared to that of Ni. The calculations also show that a CrO_2 bar should have its long axis aligned with the magnetocrystalline easy axis in order to acquire a sufficient difference of coercivities between the free and fixed layers. The dipole interaction of the CrO_2 layer is always present, however the dipole contribution is a boundary effect: by placing the nanopillar in the middle of the bar, the effects of the dipole interaction is minimized and no longer a concern for the magnetization reversal of the nanopillar.

Chapter 5

Device Fabrication

5.1 Fabrication methods

5.1.1 Selective area growth of CrO_2

Creating the nanopillar structure requires optimization of a number of processes. The optimisation of each process will be described in this chapter. Both designs require trenches wherein the CrO_2 is epitaxially grown on TiO_2. The TiO_2 substrates are cleaned in an ultrasonic bath of three different solutions; acetone, isopropanol, and demi water, in that order. Afterwards, the TiO_2 substrates are placed in a 4% aqueous hydroflouric acid (HF) solution for five minutes. The HF treatment of the TiO_2 is necessary to form high-quality terraces, which are essential in producing (100)-oriented CrO_2 growth on the TiO_2 [56][58]. The (100)-oriented CrO_2 crystals have a common magnetic easy axis in the [001]-direction, and a magnetic hard axis in the [010] direction [61][62]. Afterwards, the substrates are again cleaned in acetone, isopropanol, and demi water, and placed in an ultrasonic bath for two minutes for each cleaning step. The deep trench nanopillar design consists of a 150 nm SiO_x layer sputter-deposited on top of TiO_2 at a base pressure between 1×10^{-6} mbar and 6×10^{-6} mbar. Afterwards, the SiO_x is patterned by electron beam lithography and developed. The exposed SiO_x layer is ready to be etched by RIE. The second nanopillar design consists of a 25 nm thick layer of SiO_2 is sputter-deposited on the TiO_2 at a base pressure between 1×10^{-6} mbar and 6×10^{-6} mbar, and a sputtering pressure between 5.0×10^{-3} and 5.3×10^{-3}

mbar. The SiO_2/TiO_2 sample is now ready for electron beam lithography. A trilayer of 950K polymethyl methacrylate (PMMA) positive-tone resist is spin-coated on the SiO_2/TiO_2 sample at 4000 RPM for 90 seconds. The sample is baked at a temperature of 180° for two minutes after each spin-coating. A layer of conducting polymer is spin-coated on top of the trilayer of PMMA at 4000 RPM for 90 seconds. The sample is inserted in a Raith 100 EBPG machine for electron beam lithography. The correct dosage depends on the device design; smaller structures require a higher dose compared to bigger structures. The first lithogaphically defined layer for the CIMS consists of 50 μm by 500 μm bar connected to two 250 μm by 250 μm contact pads, with a base dose of 250 $\mu C/cm^2$. The sample is then developed in 3:1 MIBK developer. The nanopillar substrate was developed for 100 seconds. The next step involves Reactive Ion Etching (RIE) of the SiO_x layer that is left exposed after the resist development. The samples are etched in a Plasmalab 90+ system, with a mixture of CF_4:O_2 in a 3:1 ratio for 150 seconds. The etched samples are then put in acetone in an ultrasonic bath for 2 minutes to strip off the remaining PMMA resist. After stripping the remaining PMMA, the sample is cleaned by putting it again in an ultrasonic bath for 2 minutes in an isopropanol solution. The next step involves selective area growth of CrO_2.

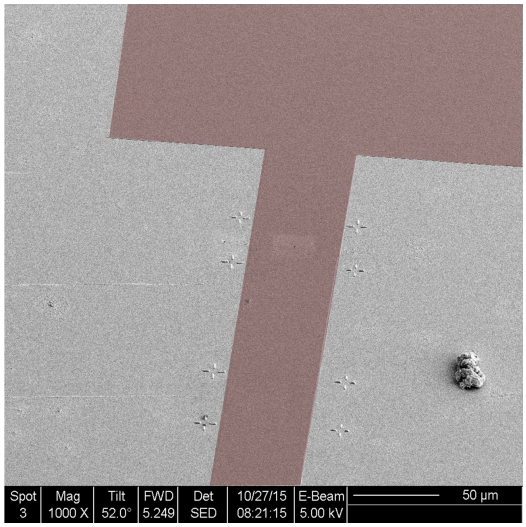

Figure 5.1: *SEM image of 50 μm by 500 μm bar connected to two contact pads (only one contact pad displayed).*

Chemical vapour deposition (CVD) occurs in a two-zone furnace. Chromium trioxide (CrO_3) is used as a precursor and oxygen is used as a carrier gas to transport the precursor from the source region to the substrate region. The CrO_3 decomposes selectively on the TiO_2 to form CrO_2. The source temperature is kept at 295° C , and the substrate temperature is kept at 360°C [63]. In Figure 5.1 a scanning electron microscopy (SEM) image of the CrO_2 bar can be seen.

5.1.2 Deep trench nanopillar

For convenience, the optimization of the process parameters is done on Si substrates. One layer of a positive tone SX AR/P 6200/2 resist is spin-coated at 4000 RPM on the SiO_x and baked at 150° for 180 seconds. A dose test of 2 $\mu C/cm^2$ to 200 $\mu C/cm^2$ is used to determine the correct dose. All the bars had a length of 30μm and widths between 4μm - 100 nm. The sample is developed in an AR 600-546 developer for up to three minutes and thirty seconds. The sample is subsequently placed in the Plasmalab 90+ reactive ion etcher using a 3:1 mixture of CF_4: O_2 procedure. However, due to the thick SiO_x layer a relatively long etching time is required, of the order of 8-10 minutes. The resist is completely stripped off during the etching procedure, exposing the SiO_x. It soon became clear that to selectively etch the SiO_x layer a hard mask is required. In the beginning a 5 nm Cu hard mask is used. The Cu is sputter-deposited on top of the SiO_x. Afterwards, the same lithography procedure is followed as before. After development, the sample is placed in an Ar-ion etcher to remove the exposed Cu. The Cu is etched at a voltage of 350 V for 40 seconds at a beam current betwen 9.0 mA-10.0 mA. Most of the resist remains and the sample is then ready for RIE. The same reactive-ion-etching procedure is used as before the inclusion of the Cu hard mask. In Figure 5.2 an AFM height profile, along with a graph dealing the depth of the trench, of a sample that was etched for eight minutes in the Plasmalab can be seen.

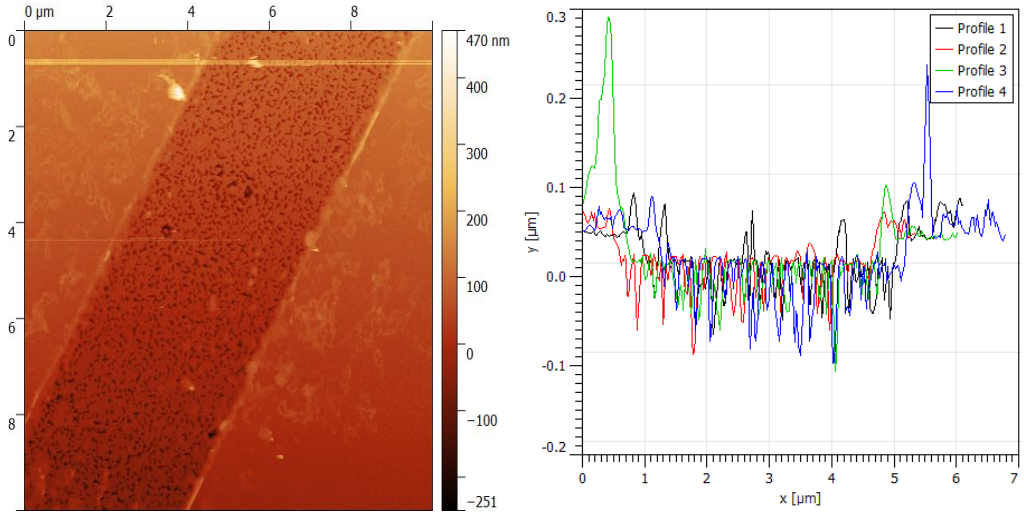

(a) ***(b)***

Figure 5.2: *AFM height profile of a deep trench design covered with a Cu hard mask. Grains in the height profile correspond to differences in height in the bottom of the trench.*

The trenches in Figure 5.2 are quite rough. The trenches have a depth of around 60 nm, and the bottom of the trench had a roughness in the order of 20 nm. The roughness of the bottom of the trench can be seen by observing the graininess of the height profile. The roughness can be attributed to the fact that Cu forms relatively large grains and so Ar-etching does not uniformly etch the Cu layer, which results in Cu residue being deposited at the edges of the trench, which in turn leads to non-uniform etching of the SiO_x. The non-uniform etching of the SiO_x results in a rough trench bottom, which hinders growth of CrO_2 on the TiO_2 substrate. The grains were on the order of tens of nanometers in height. On the edge of the trench 'ears' are also observed. The ears are a result of redeposition during Ar-etching. The height of the ears varied between 60-100 nm. In light of these problems Cu was deemed not suitable for a hard mask. The next favourable candidate for a hard mask is Al. It is known that Al forms a smooth layer: Al grains are much smaller than Cu grains. The procedure for the Al mask is the same as with the Cu mask: 5 nm of Al is sputter-deposited on top of the thick layer of SiO_x and the lithography and At-etching procedure are the same. Figure 5.3 AFM images and AFM height profiles can be seen for trenches made with the Al mask.

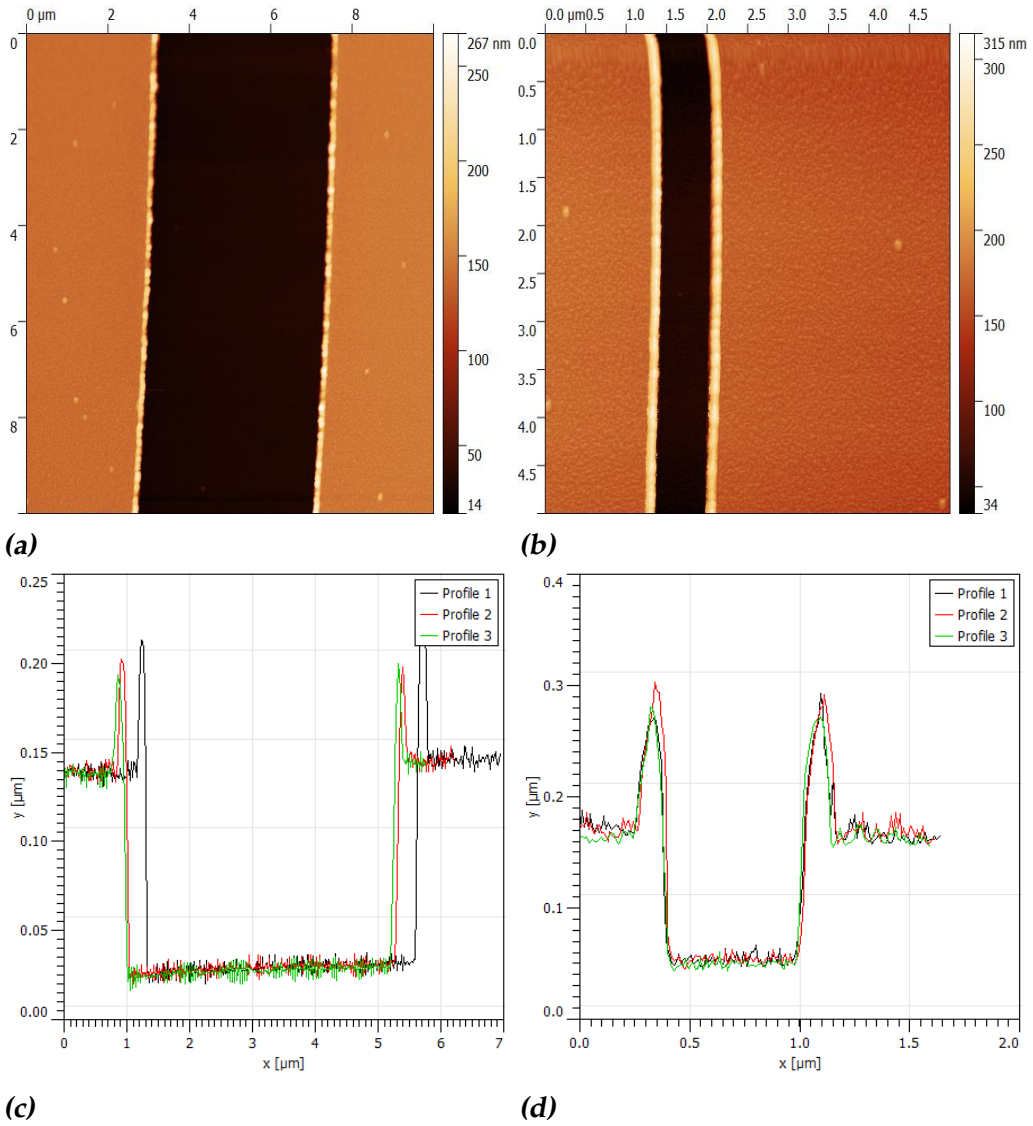

Figure 5.3: ***(a)****: AFM height profile of a 4µm wide bar made with a dose of 176 µC/cm^2* ***(b)****: AFM height profile of a 500 nm wide bar made with a dose of 190 µC/cm^2* ***(c)****: height graph of Figure 5.3a. The trench is quite well defined, however ears in of the order of 60 nm can be seen at the edges of the trench.* ***(d)****: height graph of Figure 5.3b. The trench is quite well defined, however ears in of the order of 100 nm can be seen at the edges of the trench.*

The bottom of the trenches made with the Al hard mask are smoother compared to those made with the Cu hard mask. With AFM it was confirmed that the roughness was on the order of 5 nm, which can be seen in Figure 5.3. One disturbing feature is the presence of ears, on the order of 100 nm

in height for the 500 nm wide trench, and 60 nm in height for the 4μm wide bar. In principle, the ears could be reduced by using FIB. Before trying to get rid of the ears CrO_2 was grown inside trenches of SiO_x/TiO_2 samples to confirm whether the trenches were suitable for CrO_2 growth. In Figure 5.4 AFM images of trenches with CrO_2 grown at the bottom are shown.

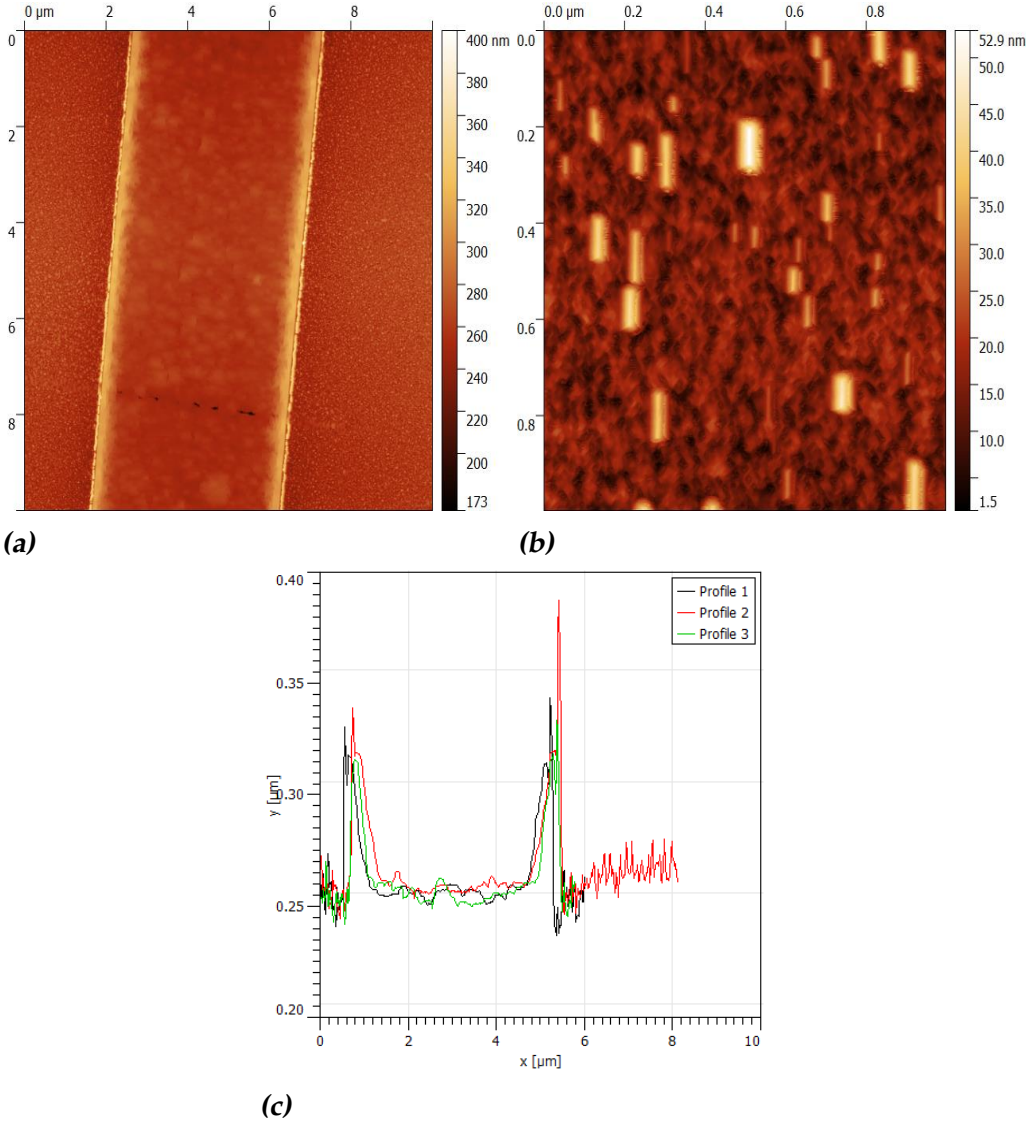

Figure 5.4: *Height profiles of trenches made with an Al mask after CrO_2 growth.*

Figure 5.4b is a zoomed in AFM image of the bottom of a deep trench design after CrO_2 growth, and grains of CrO_2 can be seen. The depth of the

trenches were measured with AFM before and after CrO_2 growth and it was determined that there was a 100 nm thick layer of CrO_2 grown in the bottom of the trench. While the bottom of the trenches were quite smooth and suitable for CrO_2 growth, the ears still appeared, and are on the order of 100 nm in height. Deep RIE also did not give reproducible results: although the parameters for RIE were kept the same, the depths of the trenches were not the same, ranging from 120 nm to 200 nm. Another serious problem comes from the design of the deep trench itself: the deep trench nanopillar design will not form discontinuous layers between the Ni layers in the trench and on the edges of the trench. An undercut is needed to form the discontinuous layers, as was mentioned in chapter 3 (see Figure 3.3). The absence of an undercut, the unpredictable ear formation, and inconsistent trench depths lead to abandoning the deep trench nanopillar design in favour of the wet-etching nanopillar design.

5.1.3 Nanostencil treatment

We now discuss the fabrication process of the second nanopillar design. After selective area growth of CrO_2 a 2 μm by 2 μm Cu layer is deposited on top of the CrO_2 bar. This sectionis concerned with the undercut needed for the formation of the nanopillar. The first step in forming the undercut is deposition of a 200 nm thick layer of SiO_x on top of the CrO_2 followed by deposition of a 10 nm thick Pt mask. Holes are made in the Pt mask and the SiO_x is etched by using an aqueous HF solution to form the undercut. The processes of making the holes in the Pt mask and the HF etching need to be optimized. Optimization of the hole formation and HF etching was done by depositing a trilayer of Pt(15nm)/SiO_x(200nm)/Pt(10nm) on substrates cut from a Si wafer. The bottom Pt layer is used to stop the HF from etching the Si substrate. The bottom Pt layer will be later replaced by a 5 nm thick Cu layer in a real device. The Si substrates are cleaned by placing the substrates two minutes in acetone and two minutes in isopropanol. After cleaning the trilayer Pt(15nm)/SiO_x(200nm)/Pt(10nm) is sputter-deposited on the Si substrates at a base and sputtering pressure similar to those of the deposition of the 25 nm SiO_x layer described in the previous section. The holes in the Pt mask are made by a combination of electron beam lithography and Ar-ion etching. One layer of 950K PMMA was spin coated at 4000 RPM for 90 seconds and baked at 180° for one minute. A base dose of 250 $\mu C/cm^2$ is used to pattern the holes in the resist. After patterning the substrates are developed in 3:1 MIBK for two

minutes. The substrates are subsequently put into an Ar-ion etcher and etched for two minutes at a beam current of 9.0 mA. After Ar-ion etching the substrates are placed in acetone to strip off the remaining PMMA. The substrates are now ready to be wet-etched with HF. In Figure 5.5 SEM images of the wet-etched samples are shown. Different etching times and concentrations of HF are used to determine the optimal parameters for forming an adequate undercut.

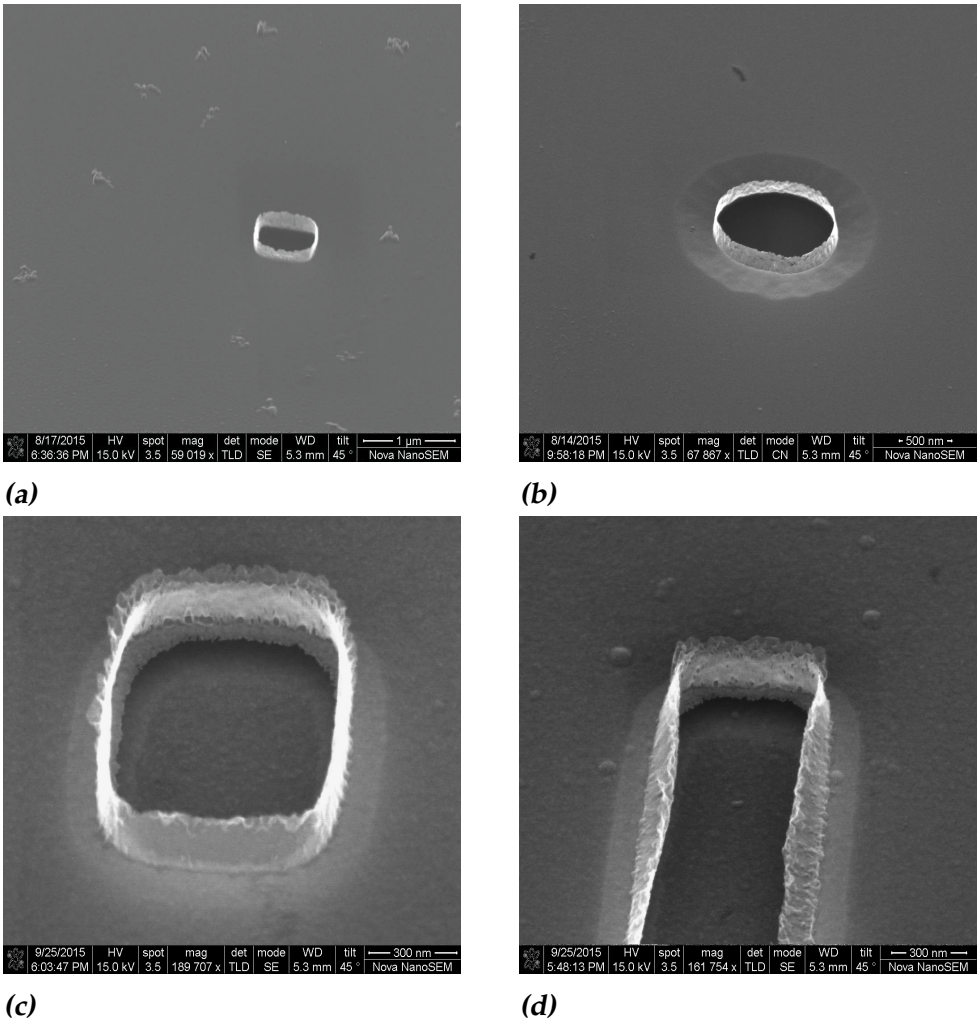

(a) ***(b)***

(c) ***(d)***

Figure 5.5: *SEM images of holes made in a Pt nanostencil and etched with an HF solution.* ***(a)*** *hole in the Pt before wet-etching.* ***(b)****: wet-etched in 12.5% HF for 90 seconds.* ***(c)****,* ***(d)****: wet-etched in 2% HF for 3 minutes .*

A crown is formed at the edges for all the samples. The crowns are due to redeposition of Pt on the side of the walls of the PMMA mask during Ar-ion etching. The crowns due to Ar-ion etching are a problem, as they are around 100 nm in height. In Figure 5.5b the undercut did not form: the top Pt layer has collapsed and is in contact with the bottom Pt layer. A less aggressive wet-etching procedure is required to form the desired undercut. In Figure 5.5c and Figure 5.5d Pt(15nm)/SiO_x(200nm)/Pt(10nm) samples were etched for three minutes with a 2% HF solution. It can be seen that an undercut has formed, on the order of 90 nm. However, the undercuts in Figure 5.5c and Figure 5.5d are not sufficient. A good undercut is required to ensure that later deposition of layers will be discontinuous, e.g. the Ni layer deposited in the cavity is not connected to the Ni layer on top of the Pt nanostencil. A slightly more aggressive HF-treatment is used, and after a few tries it was found that etching with a 4% HF solution and an etching time of two minutes and thirty seconds was optimal. We now focus on eliminating the crown formed during Ar-etching. The crown problem can be attributed to backscattering of the sputtered material with the PMMA[64]. The crown problem was solved by switching to focused-ion-beam (FIB) milling, since FIB does not require a PMMA mask[65].

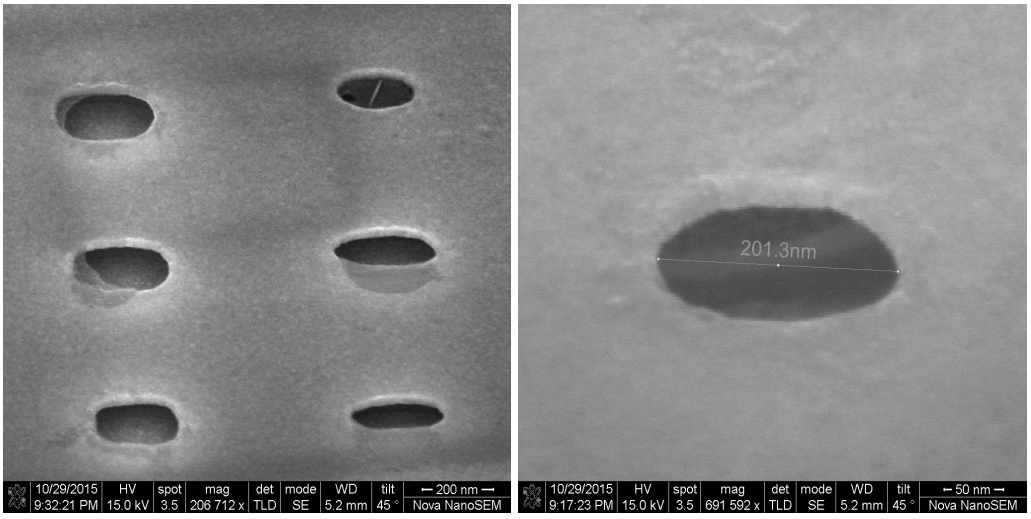

(a) ***(b)***

Figure 5.6: *SEM images of one Pt(15nm)/SiO_x(200nm)/Pt(10nm) sample with elliptical holes formed in the top Pt layer by FIB-milling. The sample was placed in a solution of 4% HF for two minutes and thirty seconds.* ***(a)*** *close up of FIB-milled holes in the top Pt layer.* ***(b)*** *zoomed-in image of the FIB-milled holes illustrating the undercut due to HF etching.*

In Figure 5.6 FIB-milled holes in a Pt(15nm)/SiO_x(200nm)/Pt(10nm) sample which was wet-etched with 4% HF solution are shown. High quality holes can be made in the Pt with dimensions as small as 50 nm, as shown in figure 5.6a. A 10 pA beam current was used in producing the holes in Figure 5.6. The sample is tilted at 45° to show that there is no redeposition at the edges of the holes. In Figure 5.6b the undercut of the holes in Figure 5.6a can be seen. Remarkably, although the undercut extends over a micron in the SiO_2, the Pt mask did not collapse, indicating that the HF-etching procedure used produces a satisfactory undercut. The next optimization step is making electrical contact with the CrO_2 layer.

5.1.4 Contact with CrO_2

Now that the procedures for producing a nanostencil and undercut have been optimized, we go back to fabrication of the CIMS device. To recap: a trench in a 25 nm thick SiO_x is made with electron lithography and CrO_2 is epitaxially grown in the trench. After the CrO_2 growth the next lithography step concerns making contact with the CrO_2 via a lift-off procedure. A bilayer of PMMA with different molecular weights is used. Both layers are spin-coated at 4000 RPM for 90 seconds and baked for one minute at a temperature of 180°. The bottom layer PMMA has a molecular weight of 600 K and the top layer has a molecular weight of 950 K. A layer of conducting polymer is spin coated at 4000 RPM for 90 seconds on top of the PMMA bilayers. 2 μm $\times$ 2 μm square structures were patterned in the middle of the CrO_2 bars at a dose of 360 $\mu C/cm^2$, along with markers. The markers are needed to help find the structures after deposition of the 200 nm of SiO_2. The sample is developed for 2 minutes in a 3:1 MIBK solution for one minute. The structure is then put in the Z-400 system for Cu deposition. Before Cu is deposited, the CrO_2 is plasma-etched in the Z-400 to remove the Cr_2O_3 oxide layer on top of the CrO_2. The CrO_2 was etched at an incident power of 50W for three minutes at a pressure of 5.0×10^{-3} mbar. After CrO_2 etching, a 10 nm thick layer of Cu is sputter-deposited on the sample. The sample is then put in acetone in an ultrasonic bath for two minutes for lift-off. The Cu layer on top of the PMMA is stripped along with the PMMA during lift-off. After stripping the PMMA the sample is ready for sputter-deposition of the SiO_x(200nm)/Pt(10nm) layers. In Figure 5.7a the markers and Cu square can be seen. In Figure 5.7b a close up of the Cu square with a 120 nm by 200 nm ellipse-shaped hole in the Pt nanostencil is shown.

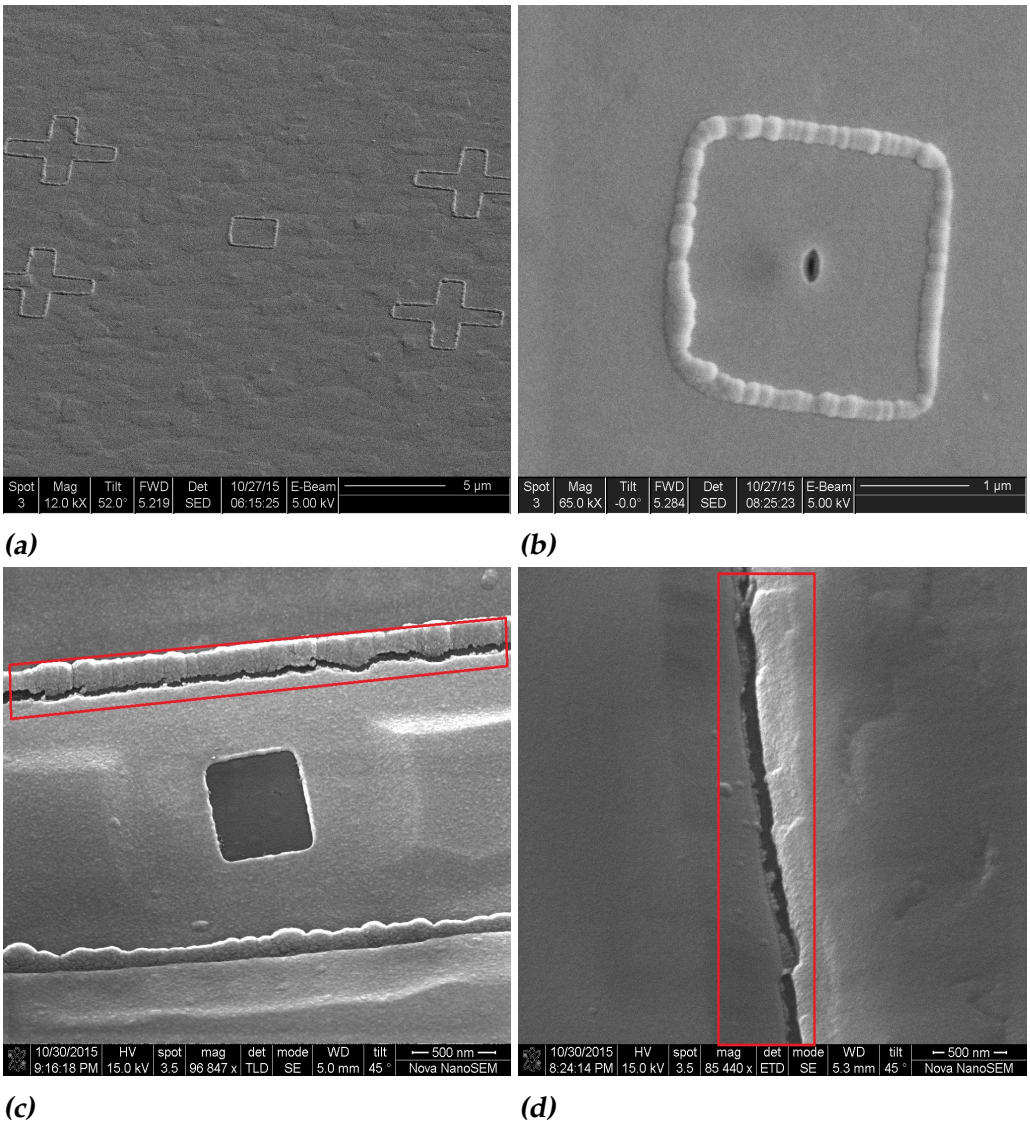

(a) ***(b)***

(c) ***(d)***

Figure 5.7: *SEM images of the Cu square structures lying below the 200nm SiO_2/Pt* ***(a)*** ***(b)****:After FIB before wet-etching.* ***(c)****,* ***(d)****: after wet-etching.*

In Figure 5.7b and Figure 5.7a the Cu structures are quite visible after sputter-deposition of the SiO_x(200nm)/Pt(10nm) layers. After sputter-deposition the sample was placed in a 4% HF solution for two minutes, the results of which are shown in Figure 5.7c and Figure 5.7d. After wet-etching it is clear that there are cracks in the Pt layer above the Cu squares, but also along the edges of the CrO_2 bar. The nanocracks are responsible for the collapse of the Pt layer in Figure 5.7c and for damage to under-

laying CrO_2 structures due to HF-etching. The nanocracks in the Pt layer along the CrO_2 are due to the height difference between the CrO_2 and substrate, while the cracks in the Pt layer on top of the Cu structures are due to an inefficient lift-off procedure of the Cu layer before sputter-deposition of the SiO_x(200nm)/Pt(10nm) layers. The cracks along the CrO_2 bar can be sealed by FIB-induced deposition [65] of Pt along the sides of the CrO_2 bar. The cracks above the Cu structure are due to an insufficient undercut that is formed during the lift-off procedure. The cracks along the Cu structures can be avoided by optimizing the undercut in the bilayer of PMMA, i.e. carrying out a dose test. In addition to a dose test, the bottom layer of 600K PMMA is replaced with a layer of 200K PMMA. The higher the molecular weight of the PMMA, the longer it takes to strip off the PMMA. The 200K PMMA will be stripped of much faster than the 950K layer on top, which leads to a larger undercut as compared to the 600K/950K bilayer. In Figure 5.8a and Figure 5.8b a dose test of the Cu circles, with radius of 2 μm is shown.

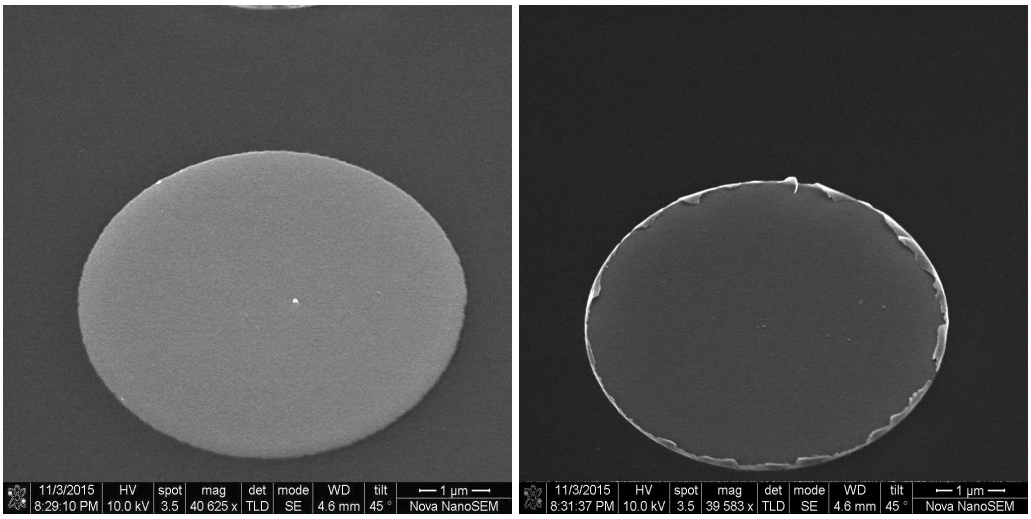

(a) ***(b)***

Figure 5.8: *Cu lift off for circular structures.* ***(a)****: 5 μm radius and dose of 435 $\mu C/cm^2$.* ***(b)****: 2μm radius and dose of 480 $\mu C/cm^2$.*

The dose test range is from 150 μC/cm^2 to 1500μC/cm^2. For higher doses the lift off procedures produces irregularly shaped Cu structures (not shown here). In Figure 5.8a it can be seen that the lift-off procedure produced a Cu structure with sharply defined edges. It is concluded that a dose in the 400-480 μC/cm^2 range produced similar results of a clean break of the Cu

during lift-off. The last steps in creating a CIMS device are deposition of the remaining ferromagnetic and electrical conductance layers, which will be discussed in the next section.

5.1.5 Capping layer

After making contact with the CrO_2 layer and using a Pt nanostencil to create a cavity in the SiO_2 we now arrive at deposition of the final nanopillar layers. Figure 5.9 is a cross section made by FIB-milling of an HF etched sample of $Pt/SiO_2/Pt$. A layer of 250 nm thick Cu was sputter-deposited on the sample. In Figure 5.9 the clogging of the gap can be seen. Due to clogging of the hole in the Pt mask instead of a desired nanopillar structure there forms an undesired nanohill structure[66].

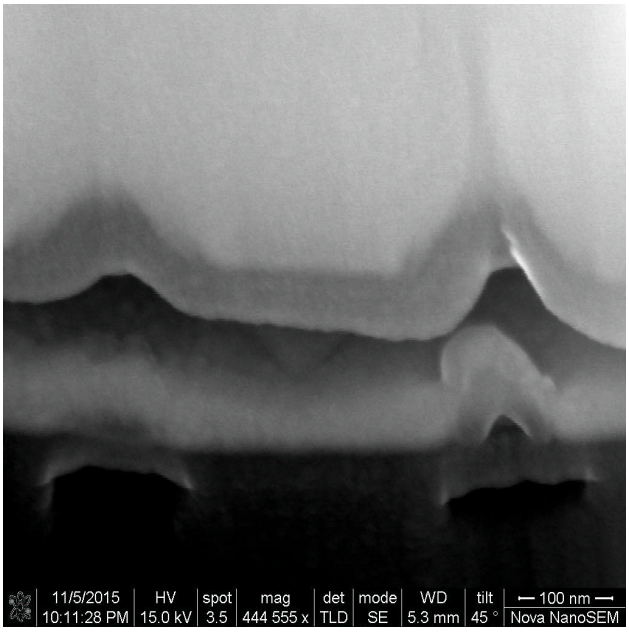

Figure 5.9: *SEM cross section after deposition of 250 nm of Cu capping layer. The effects of clogging and blurring can be seen due to the nanopillar being incomplete, while also being broadened at the base w.r.t. the Pt mask aperture.*

Another major problem for the deposition of the final layers of the nanopillar is blurring. Blurring occurs due to the way that the deposited material on the Cu layer is affected by the presence of an aperture in the Pt mask: while the sputter-deposited material on top of the Cu structures has the

shape of the mask aperture, the layer of deposited material does not have the same dimensions as the mask aperture. Clogging concerns the closing of the mask aperture by the sputter-deposited material. While blurring is not a problem when depositing the Ni layer, it does become a problem when depositing the rest of the nanopillar. Blurring is caused by two main factors. The first factor is due to the geometry of the deposition system. The material that is sputter-deposited reaches the gap in the mask from all directions. As can be seen in Figure 5.10, material that reaches the sample surface at an angle w.r.t. the surface normal causes the spread in material at the bottom of the cavity in the SiO_x layer, which results in he base of the nanopillar becoming wider than the hole in the Pt mask.

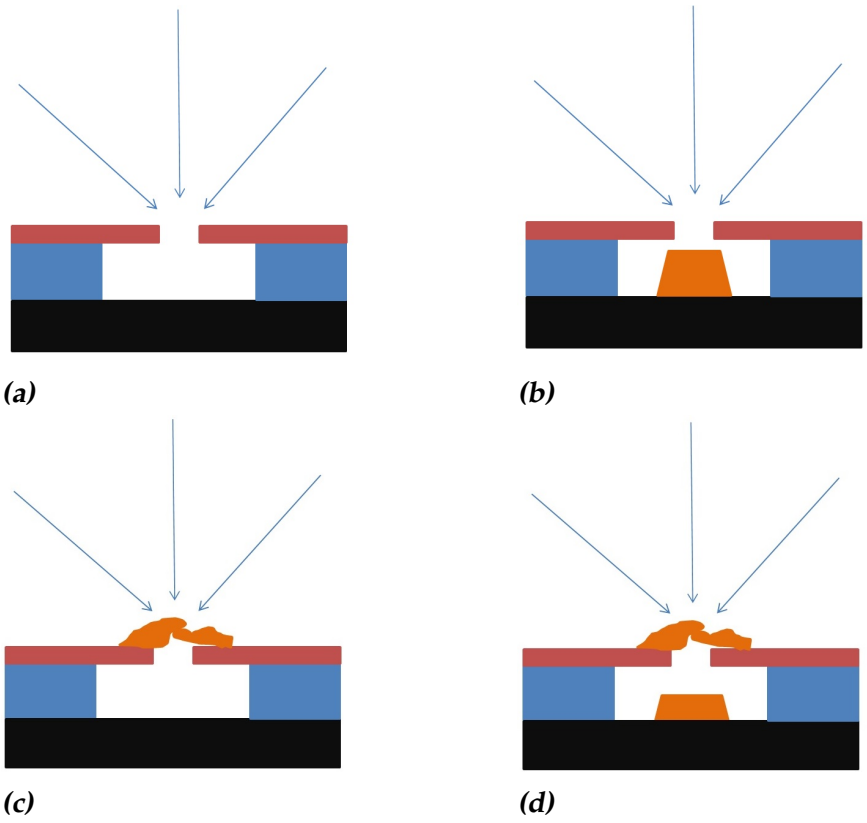

Figure 5.10: *Deposited atoms reach the aperture from all directions.* ***(b)*** *Due to blurring the base of the nanopillar becomes wider than the mask aperture.* ***c*** *Clogging of the aperture due to isotropic sputter-deposition impedes the forming of the nanopillar in the undercut.* ***d*** *The undesired combination of clogging and blurring leaves a nanopillar that does not reach the Pt mask and a nanopillar base that is wider than the mask aperture.*

The blurring, i.e. the pattern size enlargement w.r.t. the aperture size is proportional to the gap size of the aperture G, the size of the source S, and inversely proportional to the vertical distance between the source and sample surface D.

$$B \propto \frac{GS}{D} \tag{5.1}$$

As was mentioned before, blurring is not a problem when depositing the Ni layer. However, for the capping layer blurring may cause a short circuit: the capping layers that are deposited on top of the Ni layer can spread out and eventually reach the Cu square. A second contributing factor concerns surface diffusion of the deposited material. The surface diffusion is a factor that cannot be easily controlled and will not be discussed in this work. The second problem arising from the sputter-deposition geometry is clogging. Adhesion of the deposited material on the edges of the aperture will eventually fill up the gap and material will no longer be deposited in the nanopillar cavity. One solution to the blurring and clogging problem is the use of evaporative deposition, where the mean free paths of the evaporated atoms are extremely large $\sim$ 1m [66] [67]. The large mean free paths indicates that the evaporated atoms travel in a straight line from the source to the sample, reducing the blurring and the clogging. However, etching is not possible in an evaporative deposition process: after wet-etching with HF the Cu layer has to be cleaned, i.e. plasma etched. One solution is to deposit a thin protective layer on top of the Cu after plasma cleaning in the Z-400 system. After deposition of the thin layer the sample can be placed in the resistance evaporator system. A very useful protective layer which can be used is a 2 nm thick Ag layer. Silver has a long spin-diffusion length on the order of 100 nm at room temperature, and almost a micron for low temperatures. [49]. In addition to having a long spin-diffusion length, Ag is also transparent for incoming spins: spin-flipping will not occur at the Cu/Ag interface. Ag does not oxidize, however it does form a AgS layer. The formation of AgS layer is not much of a problem as it does not form very easily under atmospheric conditions. Another solution consists of placing a collimator between the source and the sample in the sputter-deposition chamber, such as the one schematically shown in Figure 5.11

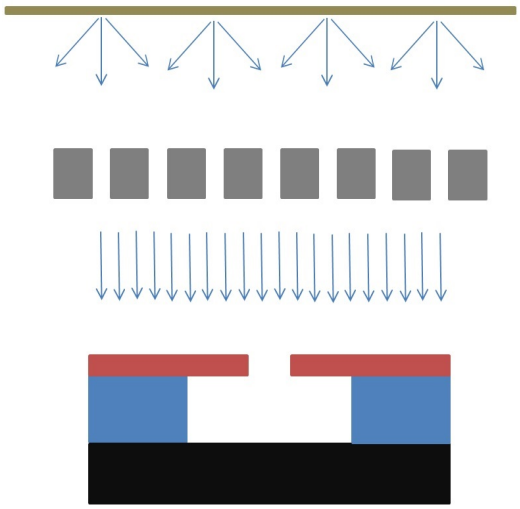

Figure 5.11: *A collimator, seen here in grey, is placed between the deposition source and the Pt mask. Atoms from the deposition source are collimated and reach the Pt mask parallel w.r.t. atoms leaving the other slits in the collimator.*

The collimator will be made from a bar wherein slits are made. The slits ensure collimation of the deposited atoms: the source of material to be deposited effectively becomes many point sources due to the slits, making the blurring formula Eq. 5.1 no longer valid. However, small overlap between atoms from different slits will be needed to ensure that a uniform layer is deposited on the sample, instead of the slit pattern. This can be done by creating a collimator with a high aspect ratio. One more consideration for the collimator is the placement. The collimator can be placed inside the Z-400 system to collimate the atoms needed for the capping layer of the nanopillar, however it cannot be placed inside the same chamber as the CIMS sample while plasma cleaning of the Cu spacer layer. To circumvent this problem, the collimator can be placed in front of the source material (connected to the source material) and not on the sample stage. With the collimator connected to the sputter source, the sample can be plasma cleaned in one chamber. Afterwards, without breaking the vacuum, the remaining nanopillar layers can be sputter-deposited. However, the use of a collimator will heavily reduce the deposition rate. As a consequence, the deposition rate due to the collimator needs to be determined. One last consideration in the final fabrication steps of the nanopillar structure concerns the capping layer. As was discussed in Chapter 2, a capping layer has a non-trivial effect on the CIMS dynamics. A capping layer with a strong spin relaxation causes a higher spin-polarization in the spacer

layer, which results in a lower critical current density needed to switch the free layer [42] [43]. The lower critical current density due to the capping layer is a theoretical bonus, as the capping layer has a more practical use. A gold capping layer has the advantage that the gold does not oxidize. The problem of oxidation occurs when depositing the final layers of the nanopillar. It was originally planned to use only Cu for the final layer of the nanopillar structure. The idea of making the capping layer out of Cu and Au stems from the combination of clogging, blurring, and oxidation. One could in principle make the entire capping layer out of gold, since it is important that in the spacer layer the spin-relaxation should be kept at a minimum. The final capping layer composition will eventually be determined by the effectiveness of the collimator. After the final layer is deposited, the final step in creating a CIMS structure is shaping the contact pads on top. The contact pads can be lithographically defined and a lift-off procedure can be used to get rid of the extra material, or a wet-etching procedure can be used.

Chapter 6

Conclusions and Outlook

We worked on optimizing the fabrication of a CIMS device which uses the half-metallic ferromagnet CrO_2 as a fixed magnetic layer. One design of a deep trench nanopillar consisted of depositing the nanopillar layers along the side of a 150 nm deep trench in SiO_2. The deep trench design was ultimately abandoned due to an insufficient undercut which is essential for depositing a well defined magnetic layer. A second nanopillar design does incorporate an undercut. The second nanopillar design consisted of depositing a bilayer of SiO_x/Pt on top of the CrO_2. A cavity is formed by milling a hole in the Pt layer and subsequently wet-etching the SiO_x layer with an aqueous HF solution. Elliptical holes in the Pt layer were made by FIB and had dimensions as small as 50 nm along the minor axis and 150 nm along the major axis of the elliptical holes. To acquire an adequate undercut the wet-etching parameters, i.e. HF solution and etch time, were optimized. The deposition of the final layers of the nanopillar turned out to not be trivial due to blurring and clogging associated with sputter deposition. This can be resolved by using a more anisotropic deposition technique like evaporative deposition. However, a setup is required where cleaning of the Cu on top of the CrO_2 and evaporative deposition can be done without breaking the vacuum. Alternatively, one can use Ag as a protective layer after Cu etching. Or Ag can be used instead of Cu to potentially eliminate the cleaning step altogether. The use of a collimator combined with sputter deposition might also resolve the blurring and clogging problem during deposition. However, the use of a collimator will heavily reduce the etching (cleaning) and deposition rate and therefore the collimator needs to be placed in front of the desired sputter target. Using

Au as a capping layer has been shown to improve spin-transfer torque and can be incorporated in a final design. Micromagnetic calculations were also made in order to determine the coercivities of the micromagnetic configurations of CrO_2, Ni and Co. As was mentioned above, Co has a higher resistivity area product than Ni. As a consequence, Co as a free layer will give a higher signal output than Ni. However, the coercivity of Co is quite close to the coercivity of the underlying CrO_2, which is troublesome for abrupt switching of the Co layer. The calculations show that the coercivity of a Ni layer is much lower than that of Co or CrO_2. The big difference in coercivities of the fixed and free layer is optimal for abrupt switching of the Ni layer. However, it is not certain whether the low resistivity area product of Ni will hamper acquiring an adequate signal in a resistance measurement.

Version of June 8, 2016– Created June 8, 2016 - 11:27

References

[1] D.C. Matts *The Theory of Magnetism I, Statics and Dynamics*

[2] J.M.D. Coey *Magnetism and Magnetic Materials*, 2010

[3] Atsufumi Hirohata and Koki Takanashi *Future perspectives for spintronic devices*, Journal of Physics D: Applied Physics, Volume 47, Number 19

[4] D.C. Ralph and M.D. Stiles *Spin transfer torques*, Journal of Magnetism and Magnetic Materials, 320 (2008), 1190-1216

[5] M.N. Baibich, J.M. Broto, A. Fert, F. Nguyen Van Dau, F. Petroff, P. Eitenne, G. Creuzet, A. Friederich, and J. Chazelas *Giant Magnetoresistance of (001) Fe/(001) Cr Magnetic Superlattices*, Physical Review Letters, Volume 61, Number 21, (1988)

[6] Maxim Tsoi *Spin-torque measured up*, Nature Physics **4**, 17-18 (2008)

[7] N. Locatelli, V. Cros, and J. Grollier *Spin-torque building blocks*, Nature Materials, **13**, 11-20 (2014)

[8] S.I. Kiselev, J.C. Sankey, I.N. Krivorotov, N.C. Emley, R.J. Schoelkopf, R.A. Buhrman, and D.C. Ralph *Microwave oscillations of a nanomagnet driven by a spin-polarized current*, Nature **425**, 380-383,

[9] F.J. Jedema, H.B. Heersche, A.T. Filip, J.J.A. Baselmans, and B.J. van Wees *Electrical detection of spin precession in a metallic mesoscopic spin valve*, Nature **416**, 713-716

[10] H. Szambolics, J.-Ch. Toussaint, A. Marty, I.M. Miron, L.D. Buda-Prejbeanu *Domain wall motion in ferromagnetic systems with perpendicular magnetization*, Journal of Magnetism and Magnetic Materials 321(2009) 1912-1918

[11] L.J. McGilly, P. Yudin, L. Feigl, A.K. Tagantsev and N. Setter *Controlling domain wall motion in ferroelectric thin films*, Nature Nanotechnology 10, 145-150 (2015)

[12] J.Z. Sun *Spin-current interaction with a mono domain magnetic body: A model study*, Physical Review B, Volume 62, Number 1

[13] J. Slonczewski*Current-driven excitation of magnetic multilayers*, Journal of Magnetism and Magnetic Materials 159, L1 - L7, (1996)

[14] L. Berger , Physical Review B **54**, 9353 (1996)

[15] K. Yagami, A.A. Tulapurkar, A. Fukushima, and Y. Suzuki *Low-current spin-transfer switching and its thermal durability in a low-saturation magnetization nanomagnet* Applied Physics Letters **85**, 5634 (2004)

[16] F.J. Albert, N.C. Emley, E.B. Myers, D.C. Ralph, and R.A. Buhrman *Quantitative Study of Magnetization Reversal by Spin-Polarized Current in Magnetic Multilayer Nanopillars*, Physical Review Letters, Volume 89, Number 22

[17] Hiroaki Sukegawa, Shinya Kasai, Takao Furubayashi, Seiji Mitani, and Koichiro Inomata *Spin-transfer switching in an epitaxial spin-valve nanopillar with a full-Heusler $Co_2FeAl_{0.5}Si_{0.5}$ alloy*, Applied Physics Letters **96**, 042508 (2010)

[18] D. van Delft and P. Kes *The discovery of superconductivity*, Physics Today **63**, 38 (2010)

[19] James F. Annet *Superconductivity, Superfluids and Condensates*, Oxford University Press, 2003.

[20] L.D. Landau, E.M. Lifshitz and L.P. Pitaevskii *Electrodynamics of Continuous Media, 2nd Edition*

[21] Mathias Eschrig *Spin-polarized supercurrents for spintronics*, Physics Today **64**, 43 (2011)

[22] R.S. Keixer, S.T.B. Goennenwein, T.M. Klapwijk, G. Miao, G. Xiao, and A. Gupta *A spin triplet supercurrent through the half-metallic ferromagnet CrO_2*, Nature **439**, 825 (2006)

[23] Jacob Linder and Jason W.A. Robinson *Superconducting spintronics*, Nature Physics **11**, 307-315 (2015)

[24] A. Singh, C. Jansen, K. Lahabi, J. Aarts *Growth of half-metallic CrO_2 nanostructures for superconducting spintronic applications* arXiv:1603.02675

[25] David J. Griffiths *Introduction to electrodynamics, Third Edition*

[26] David J. Griffiths *Introduction to Quantum Mechanics, Second Edition*

[27] Assa Auerbach *Interacting electrons and quantum magnetism*

[28] Harald Ibach and Hans Lüth *Solid-State Physics, An Introduction to Principles of Materials Science*

[29] W.J. Duffin *Electricity and Magnetism, Fourth Edition*

[30] Jan Zaanen *The classical condensates, from Crystals to Fermi-liquids*, Lorentz Institute for Theoretical Physics, Department of Physics and Astronomy, University of Leiden

[31] Tôru Moriya *Theory of itinerant magnetism*, Journal of Magnetism and Magnetic Materials 100 (1991), 261-271

[32] Karlheinz Schwarz *CrO_2 predicted as a half-metallic ferromagnet*, Journal of Physics F: Metal Physics, **16** (1986), L211-215

[33] J.M.D Coey *Half-metallic ferromagnetism: Example of CrO_2 (invited)*, Journal of Applied Physics, Volume 91, Number 10

[34] Steven P. Lewis, Philip B. Allen, and Taizo Sasaki *Band structure and transport properties of CrO_2*, Physical Review B **55**, 10253

[35] C.M. Hurd *Varieties of Magnetic Order in Solids*, Contemporary Physics, 1982, Vol. 23, No. **5**, 469-493

[36] R.J. Soulen Jr., J.M. Byers, M.S. Osofsky, B. Nadgorny, T. Ambrose, S.F. Cheng, P.R. Broussard, C.T. Tanaka, J. Nowak, J.S. Moodera, A. Barry, J.M.D. Coey *Measuring the Spin Polarization of a Metal with a Superconducting Point Contact*, Science **282**, 85 (1998)

[37] W.J. Desist, P.R. Broussard, T.F. Ambrose, B.E. Nadgorny, M.S. Osofsky *Highly spin-polarized chromium dioxide thin films prepared by chemical vapor deposition from chromyl chloride*, Applied Physics Letters **76**, 3789 (2000)

[38] Y. Ji, G.J. Strikers, F.Y. Yang, C.L. Chien, J.M. Bryers, A. Anguelouch, Gang Xiago, and A. Gupta *Determination of the Spin Polarization of Half-Metallic CrO_2 by Point Contact Andreev Reflection*, Physical Review Letters, Volume 86, Number 24

[39] C.M. Fang, G.A. de Wijs, and R.A. de Groot *Spin-polarization in half-metals (invited)*, Journal of Applied Physics, Volume 91, Number 10

[40] M.D. Stiles and J. Miltat *Spin Transfer Torque and Dynamics*, chapter in *Spin Dynamics in Confined Magnetic Structures III*, volume 101 of the series Topics in Applied Physics, pp 225-308

[41] M.C. Wu, A. Aziz, M. Ali, C.H. Marrows, B.J. Hickey, Z.H. Barber, and M.G. Blamire *Reduction in critical current of current induced switching in an inhomogeneous nano magnet*, Applied Physics Letters **94**, 122511 (2009)

[42] S. Bala Kumar, S.G. Tan, M.B.A. Jalil, J. Guo, E. Girgis, and Yong Jiang *Spin transfer torque in current-perpendicular-to-plane multilayer structure induced by spin relaxation in the capping layer*, Journal of Applied Physics **103**, 07A712 (2008)

[43] T. Yang, A. Hirohata, T. Kimura, and Y. Otani *Influence of capping layer on the current-induced magnetization switching in magnetic nanopillars*, Journal of Applied Physics **99**, 073708 (2006)

[44] Nyuk Leong Chung *Theory of Spintronics in Nanostructures*, Department of Electrical and Computer Engineering, National University of Singapore, 2012

[45] P.C. van Son, H. van Kempen, and P. Wyder *Boundary Resistance of the Ferromagnetic-Nonferromagnetic Metal Interface*, Physical Review Letters, Volume 58, Number 21

[46] S. Andrews *Fabrication of magnetic nanopillars and X-ray imaging of spin-transfer phenomena*, PhD Thesis, Department of materials science and engineering, Stanford University, 2005

[47] B. Özyilmaz, G. Richter, N. Müsgens, M. Fraune, M. Hawraneck, B. Beschoten, and G. Güntherodt *Focused-ion-beam milling based nanostencil mask fabrication for spin transfer torque studies*, Journal of Applied Physics **101**, 063920, 2007

[48] Satoshi Yakata, Yasuo Ando, Terunobu Miyazaki and Shigemi Mizukami *Temperature Dependences of Spin-Diffusion Lengths of Cu and Ru layers*, Japanese Journal of Applied Physics Vol 45. No. 5A, 2006, pp. 3892-3895

[49] Jack Bass and William P. Pratt Jr. *Spin-Diffusion Lengths in Metals and Alloys, and Spin-Flipping at Metal/Metal Interfaces: an Experimentalist's*

Critical Review, Department of Physics and Astronomy, Michigan State University

[50] W.P. Sterk *Magnetisation characteristics of noncollinear ferromagnetic bilayers*, Bachelor Thesis, Leiden University 2015

[51] Josef Fidler and Thomas Schrefl *Micromagnetic modelling - the current state of the art*, Journal of Applied Physics D: Applied Physics **33** (2000) R135-R156

[52] M.J. Donahue and D.G. Porter *OOMMF User's guide*, US department of Commerce, Technology Administration, National Institute of Standards and Technology, 1999

[53] Evaggelos Kritsikis, Jean-Christophe Toussaint, Olivier Fruchart, Helga Szambolics, and Liliana Buda-Prejbeanu *Fast computation of magnetostatic fields by nonuniform fast Fourier transforms*, Applied Physics Letters **93**, 132508 (2008)

[54] Ewout Beukers *Spin-polarized superconductivity in superconductor-ferromagnet hybrids: simulations and experiment*, Bachelor Thesis, Leiden University 2015

[55] Richard P. Boardman *Computer simulation studies of magnetic nanostructures*, Faculty of Engineering, Science and Mathematics, University of Southampton

[56] Guo-Xing Miao, Gang Xiao, and Arunava Gupta *Influence of substrate treatment on the growth morphology and magnetic anisotropy of epitaxial CrO_2 films*, Physica Status Solidi (a) **203**, No. 7, 1513-1520 (2006)

[57] C. König, M. Fonin, M. Laufenberg, A. Biehler, W. Bührer, M. Kläui, U. Rüdiger, and G. Güntherodt *Micromagnetism and magnetotransport properties of micron-sized epitaxial CrO_2 (100) wires*, Physical Review B **75**, 144428 (2007)

[58] B.Z. Rameev, A. Gupta, G. Miao, G. Xiao, F. Yildiz, L.R. Tagirov, and B. Aktas *The magnetic anisotropy of thin epitaxial CrO_2 films studied by ferromagnetic resonance*, Technical Physics Letters, Vol 31, No. 9, 2005, pp. 802-805

[59] Robert C. O'Handley *Modern Magnetic Materials, Principles and Applications*

[60] Xiaojing Zou and Gang Xiao *Magnetic domain configurations of epitaxial chromium dioxide (CrO_2) nanostructure*, Applied Physics Letters **91**, 113512 (2007)

[61] A. Intepe, S. Kazan, K.B. Chetry, F. Mikailzade, R. Yilgin, B. Aktas, M. Ozdemir, and A. Gupta *Magnetic resonance studies of half-metallic epitaxial CrO_2 thin films grown on differently oriented TiO_2 substrates*, Journal of Superconductivity and Novel Magnetism, December 2012, Volume 25, Issue 8, pp 2647-2651

[62] B.Z. Rameev, A. Gupta, G.X. Miao, G. Xiao, F. Yildiz, L.R. Tagirov, and B. Aktas *FMR study of strain-induced magnetic anisotropies in CrO_2 thin films*, Physica Status Solidi (a) **201**, No. 15, 3350-3353 (2004)

[63] A. Gupta, X.W. Li, S. Guha, and Gang Xiao, *Selective-area and lateral overgrowth of chromium dioxide (CrO_2) films by chemical vapour deposition*, Applied Physics Letters **75**, 2996, 1996

[64] L. Stafford, J. Margot, S. Delprat, M. Chaker, and S.J. Pearton *Influence of redeposition on the plasma etching dynamics*, Journal of Applied Physics **101**, 083303 (2007)

[65] C.A. Volkert and A.M. Minor *Focused Ion Beam Microscopy and Micromachining*, Materials Research Society, Volume 32, Issue 05, May 2007, pp 389-399

[66] O. Vasquez-Mena, L. Gross, S. Xie, L.G. Villanueva, and J. Brugger *Resistless nanofabrication by stencil lithography: A review*, Microelectronic Engineering 132 (2015) 236-254

[67] Sheila Shadidi, Bahareh Moazzenchi, and Mahmood Ghoranneviss *A review-application of physical vapour deposition (PVD) and related methods in the textile industry*, European Physical Journal of Applied Physics (2015) 71:31302